Article

Neuron

TREM2 Haplodeficiency in Mice and Humans Impairs the Microglia Barrier Function Leading to Decreased Amyloid Compaction and Severe Axonal Dystrophy

Highlights

- TREM2/DAP12 signaling regulates microglia process envelopment of amyloid plaques
- Loss of microglia envelopment in TREM2/DAP12 deficiency reduces plaque compaction
- STORM microscopy shows greater fibril branching and surface area in TREM2 deficiency
- Human R47H TREM2 variant impairs the microglia barrier and worsens axonal dystrophy

Authors

Peng Yuan, Carlo Condello, C. Dirk Keene, ..., Marco Colonna, David Baddeley, Jaime Grutzendler

Correspondence

jaime.grutzendler@yale.edu

In Brief

Yuan, Condello, et al. demonstrate that haplodeficiency of the microglia-specific gene TREM2 markedly impairs the ability of microglia to compact and insulate amyloid deposits. Loss of this neuroprotective microglia function leads to marked axonal dystrophy, potentially contributing to the increased risk of dementia for carriers of TREM2 loss-of-function mutations.

Yuan et al., 2016, Neuron *90*, 724–739
May 18, 2016
http://dx.doi.org/10.1016/j.neuron.2016.05.003

CellPress

CellPress

Neuron
Article

TREM2 Haplodeficiency in Mice and Humans Impairs the Microglia Barrier Function Leading to Decreased Amyloid Compaction and Severe Axonal Dystrophy

Peng Yuan,[1,2,9] Carlo Condello,[1,9,10] C. Dirk Keene,[3] Yaming Wang,[4] Thomas D. Bird,[5] Steven M. Paul,[6] Wenjie Luo,[6] Marco Colonna,[4] David Baddeley,[7,8] and Jaime Grutzendler[1,2,*]

[1]Department of Neurology
[2]Department of Neuroscience
Yale University, New Haven, CT 06511, USA
[3]Department of Pathology, University of Washington, Seattle, WA 98195, USA
[4]Department of Pathology and Immunology, Washington University School of Medicine, St. Louis, MO 63110, USA
[5]Department of Neurology, University of Washington, Seattle, WA 98195, USA
[6]The Helen and Robert Appel Alzheimer's Disease Research Institute, Brain and Mind Research Institute, Weill Cornell Medical College, New York, NY 10065, USA
[7]Department of Cell Biology, Yale University, New Haven, CT 06511, USA
[8]Nanobiology Institute, Yale University, West Haven, CT 06515, USA
[9]Co-first author
[10]Present address: Department of Neurology, Institute for Neurodegenerative Diseases, University of California, San Francisco, San Francisco, CA 94158, USA
*Correspondence: jaime.grutzendler@yale.edu
http://dx.doi.org/10.1016/j.neuron.2016.05.003

SUMMARY

Haplodeficiency of the microglia gene *TREM2* increases risk for late-onset Alzheimer's disease (AD) but the mechanisms remain uncertain. To investigate this, we used high-resolution confocal and super-resolution (STORM) microscopy in AD-like mice and human AD tissue. We found that microglia processes, rich in TREM2, tightly surround early amyloid fibrils and plaques promoting their compaction and insulation. In *Trem2*- or *DAP12*-haplodeficient mice and in humans with R47H *TREM2* mutations, microglia had a markedly reduced ability to envelop amyloid deposits. This led to an increase in less compact plaques with longer and branched amyloid fibrils resulting in greater surface exposure to adjacent neurites. This was associated with more severe neuritic tau hyperphosphorylation and axonal dystrophy around amyloid deposits. Thus, TREM2 deficiency may disrupt the formation of a neuroprotective microglia barrier that regulates amyloid compaction and insulation. Pharmacological modulation of this barrier could be a novel therapeutic strategy for AD.

INTRODUCTION

Microglia are the resident immune cells in the CNS, where they constantly survey their microenvironment and become activated in various neurological disorders (Davalos et al., 2005; Hanisch and Kettenmann, 2007). In Alzheimer's disease (AD), a striking feature of microglia is their universal clustering around amyloid-β (Aβ) deposits, one of the major pathological hallmarks of this condition. It has traditionally been thought that activated microglia remove Aβ deposits via phagocytosis (Lee and Landreth, 2010). However, multiple recent lines of evidence indicate that microglia are ineffective at removing fibrillar Aβ in vivo (Condello et al., 2011; Liu et al., 2010; Stalder et al., 2001). At the same time, given their ability to secrete cytokines and reactive oxygen species, microglia have the potential to be neurotoxic (Block et al., 2007). Thus, it remains unknown whether certain aspects of microglial function play beneficial or detrimental roles that could be important for disease pathogenesis.

TREM2 (Triggering Receptor Expressed on Myeloid cells 2) gene is specifically expressed by microglia in the CNS (Schmid et al., 2002). A loss-of-function R47H (rs75932628, Arginine-47-Histidine) mutation in *TREM2* constitutes one of the strongest single allele genetic risk factors for AD (Guerreiro et al., 2013; Jin et al., 2014; Jonsson et al., 2013; Korvatska et al., 2015; Ruiz et al., 2014), providing the clearest link between microglia dysfunction and AD pathogenesis. While loss of *Trem2* in vitro disrupts Aβ phagocytosis by microglia (Kleinberger et al., 2014), *Trem2*-haplodeficient AD-like mice have shown inconsistent results with respect to the amounts of cerebral Aβ deposition (Jay et al., 2015; Ulrich et al., 2014; Wang et al., 2015). Thus, it remains unclear to what extent *Trem2* regulates microglia phagocytosis in vivo, suggesting that the increased risk of AD in *Trem2* haplodeficiency may not be due to differences in amyloid plaque load. Interestingly, most studies in *Trem2*-deficient AD-like mice have shown reduced number of microglia around amyloid plaques (Jay et al., 2015; Wang et al., 2015). However, it remains unknown how subtle changes in microglia around plaques could profoundly increase the risk of AD.

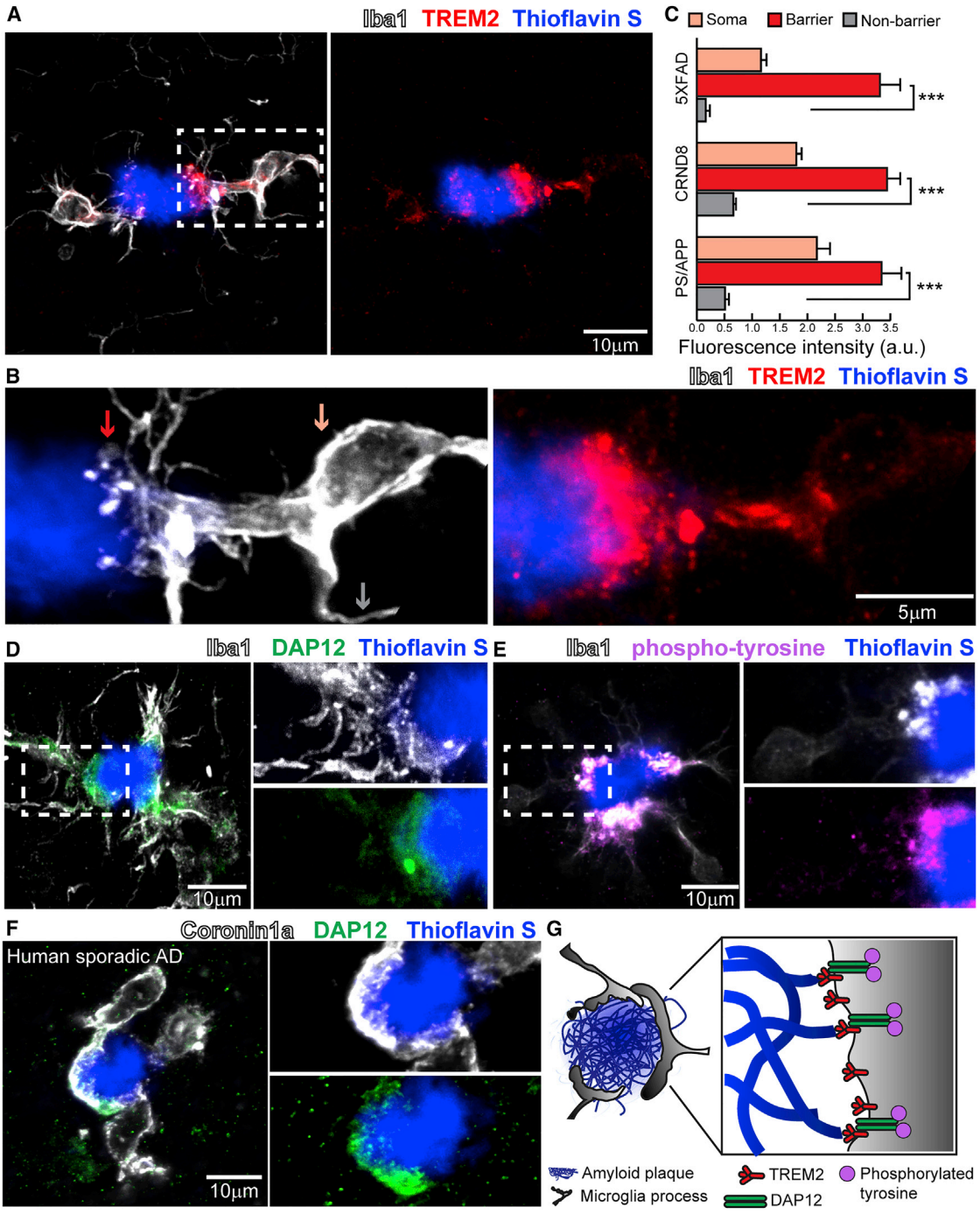

Figure 1. Trem2-Mediated Signaling Is Activated within Microglia Processes Directly Contacting Amyloid Plaques

(A) Confocal images showing the subcellular localization of immunostained Trem2 (red) within Iba1-positive microglia (white) clustered around an amyloid plaque (blue) in a *5XFAD* mouse.

(B) Zoomed images of Trem2 in plaque-associated microglia processes from the dashed box in (A). Microglia processes were divided into three subcellular compartments: (1) soma (pink arrow), (2) barrier (processes contacting plaque, red arrow), and (3) non-barrier (processes not engaged with plaque, gray arrow).

(C) Quantification of Trem2 fluorescence intensity in microglia associated with plaques in AD mouse models: *5XFAD*, *CRND8*, and *APPPS1-21*. n = 30 microglia from each model. One-way ANOVA with post hoc Tukey tests were used for statistical comparisons within mouse models, ***$p < 0.001$; a.u., arbitrary unit. Data presented as mean ± SEM.

(D and E) Confocal images showing elevated levels of immunostained-DAP12 (D, green) and phospho-tyrosine (E, magenta) at the microglia-plaque interface (white). Right: zoomed split channels from the dashed box.

(legend continued on next page)

Furthermore, it remains unclear how these mouse studies correlate with the human pathology.

Recently, we identified a protective function of microglia, whereby their processes tightly wrap around plaques and act as a physical barrier that prevents the outward extension of amyloid fibrils (Condello et al., 2015). This barrier function promotes formation of highly compact plaque microregions that have minimal affinity for soluble Aβ42 (Figure S1). Conversely, areas not covered by microglia processes display hotspots with very high soluble Aβ42 affinity, leading to markedly concentrated protofibrillar Aβ plaque regions. These Aβ hotspots are neurotoxic given that adjacent axons develop a greater extent of dystrophy compared to those next to non-hotspot regions covered by microglia (Condello et al., 2015). Despite these intriguing observations in mice, the importance of microglia in the pathogenesis of AD and more specifically the relevance of this newly discovered microglial barrier function in humans has not been demonstrated.

We thus hypothesized that disruption of the microglia barrier function is a cellular mechanism underlying association between loss-of-function *TREM2* mutations and increased risk of AD. To test this, we used quantitative high-resolution confocal microscopy and super-resolution Stochastic Optical Reconstruction Microscopy (STORM) in both human brains of patients with R47H TREM2 mutations and in AD-like mice lacking either Trem2 or its adaptor protein DNAX-binding protein of 12 kDa (DAP12). This revealed unprecedented structural detail of the landscape of amyloid fibrils, axonal dystrophy, and microglia heterogeneity around plaques in *TREM2* haplodeficiency.

Our data in mice and humans indicate that microglia processes closely interact with individual amyloid fibrils in early non-compact filamentous plaques and later form specialized protrusions rich in TREM2 and DAP12 that tightly wrap around the surface of compact plaques. We then demonstrate in both *TREM2* and *DAP12* haplodeficiency a striking microglia phenotype in which these cells fail to polarize and engage nascent amyloid fibrils and mature compact plaques. However, this was not associated with differences in amyloid phagocytosis or plaque numbers. Instead, we observed a marked reduction in amyloid plaque compaction and a subsequent increase in plaque surface area contacting neuropil, which was associated with a significant increase in the degree of axonal dystrophy. A strikingly similar phenotype was also observed in human *TREM2* R47H mutants, demonstrating that this neuroprotective microglia barrier is conserved in humans. Our data indicate that *TREM2* deficiency disrupts this specialized barrier function and may thus constitute a previously unknown cellular mechanism linking *TREM2* R47H variant with increased risk of dementia. Future studies may determine whether similar mechanisms play a role in the pathogenesis of late-onset AD associated with other microglia-related genetic risk alleles.

RESULTS

Microglia Processes Contacting Plaques Are Highly Enriched with Trem2

We first examined the expression pattern of Trem2 in the brains of three transgenic AD mouse models. Building upon previous reports (Frank et al., 2008; Lue et al., 2015; Matarin et al., 2015), high-resolution confocal microscopy revealed that Trem2 is enriched within plaque-associated microglia, but not in microglia away from plaques or other neural cells (Figure S2). Interestingly, we found that Trem2 expression was exceptionally high at the leading edges of microglia processes directly contacting amyloid plaques (Figures 1A–1C). We also detected polarized expression of its signaling adaptor protein DAP12 (Figure 1D), and a marker of phosphorylated tyrosine (Figure 1E) consistent with downstream kinase-mediated signal transduction (Colonna, 2003). Similar to mice, in postmortem human brain, we found enhanced DAP12 expression specifically polarized to microglia processes contacting amyloid plaques (Figure 1F and Table S1). The robust enrichment of Trem2, DAP12, and a marker of downstream tyrosine phosphorylation suggests that these signaling proteins could play a key role in the envelopment of the plaque surface by microglia processes and the establishment of the microglia barrier (Figure 1G).

Trem2 Haplodeficiency Abolishes the Microglia Barrier but Does Not Impair Aβ Phagocytosis

We next examined structural and functional features of microglia in AD-like transgenic mice carrying different copy numbers of the *Trem2* or *DAP12* genes (Figures 2, S2, and S4). High-resolution confocal microscopy revealed that *Trem2* or *DAP12* deletion markedly reduced the degree of plaque surface coverage by microglia processes (Figures 2A–2D). The dramatic change of plaque coverage in *Trem2* and *DAP12* deficiency cannot be explained alone by the modest ~20% reduction in the number of plaque-associated microglia (Figures S3 and S4). Instead, it appears that microglia in *Trem2* or *DAP12* deficiency have an impairment in the ability to polarize their processes toward the plaque surface and thus are unable to create an effective barrier around them (Figures 2A–2D). Interestingly, in *Trem2* deficiency, microglia processes contacting plaques did not show enrichment of phosphorylated tyrosine (Figure S3), a marker of downstream tyrosine kinase activation that is potentially necessary for triggering actin reorganization during process polarization (Peng et al., 2010). Indeed, contrary to the robust microglia processes seen in wild-type mice (Figure 2E), processes contacting plaques in either *Trem2*- or *DAP12*-deficient mice displayed characteristic dysmorphic features with fine processes and terminal loops that failed to closely track the boundaries of the plaque (Figure 2F). Thus, *Trem2* likely plays a critical role in signaling microglia process specialization underlying the formation of the microglia barrier around plaques.

(F) Confocal images of DAP12 (green) and microglia (white) in human sporadic AD postmortem brain showing strong polarization to processes contacting plaques.

(G) Diagram of specialized microglial processes wrapping around amyloid plaque microregions, with enriched TREM2 and downstream signaling proteins. All analyses were performed in mouse somatosensory cortex human middle frontal gyrus.

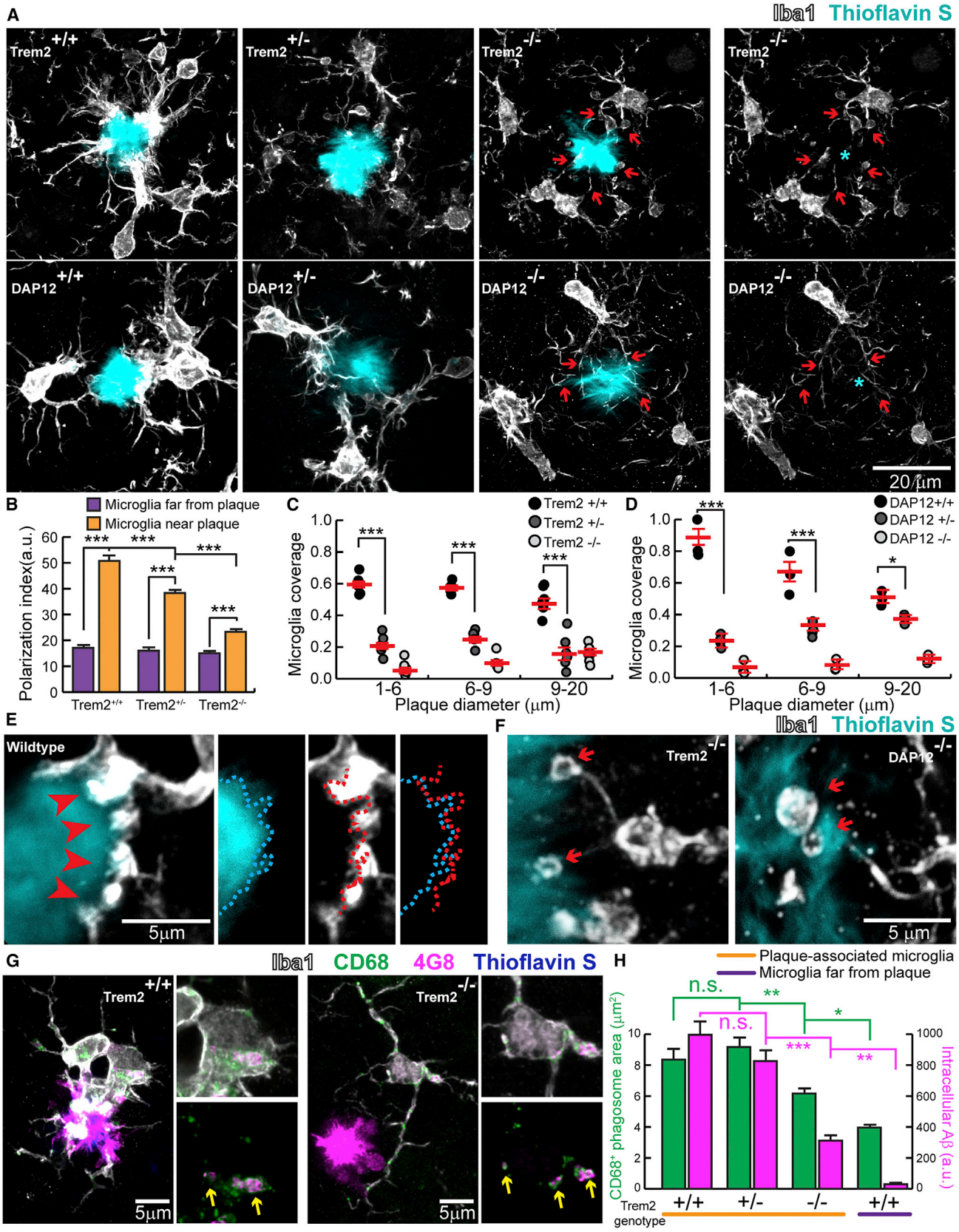

(legend on next page)

To assess whether *Trem2* deficiency also affected Aβ fibril engulfment by microglia, we performed immunohistochemistry and quantitative confocal image analysis to measure the Aβ content within CD68-immunolabeled microglial phagosomes, a correlate of Aβ phagocytosis efficiency. While in *Trem2*$^{-/-}$ mice, there was a significant reduction in Aβ phagocytosis, we were surprised to see that in *Trem2*$^{+/-}$ mice, a more relevant model of human *TREM2* haplodeficiency leading to AD, there was no significant difference in either the number of phagosomes or amount of Aβ within phagosomes (Figures 2G and 2H). This suggests that a defect in microglia phagocytosis of Aβ is not the main cause of neuropathology in *Trem2* deficiency. Instead it suggests that inability of microglia processes to polarize and establish an effective barrier may be a neuropathological mechanism in *TREM2* R47H variant carriers.

Trem2 Haplodeficiency Decreases Amyloid Plaque Compaction and Increases Total Fibril Surface Area

We next asked how deficiency in the microglia barrier may impact the structural organization of individual plaques. Quantitative confocal analyses of individual plaques labeled by the β sheet binding dye thioflavin S, in *Trem2*- and *DAP12*-deficient mice, showed a reduction in the fluorescence and a diffuse plaque morphology with amyloid fibrils projecting outward radially (Figures 3A–3C). To directly observe Aβ fibrils, we next performed super-resolution nanoscopy using stochastic optical reconstruction microscopy (STORM) in brain slices fluorescently immunolabeled with an N terminus anti-Aβ antibody. While plaques from *Trem2*$^{+/+}$ mice exhibited circumscribed borders, in *Trem2*$^{+/-}$ and *Trem2*$^{-/-}$ mice, plaques displayed spike-like fibrils extending radially (Figure 3D). We then defined three different plaque regions based on Aβ fibril organization: (1) diffuse region; (2) mesh-like region (likely formed by interweaving of individual Aβ fibrils); and (3) compact region (where densely packed fibrils limit antibody penetration (Figures 3E and S5). *Trem2* deficiency markedly increased the proportion of diffuse fibrils and decreased the proportion of mesh-like and compact fibrils (Figure 3F). Furthermore, loss of *Trem2* increased the average length of diffuse fibrils radiating outward from the mesh-like compact core (Figures 3G and 3H) (average 231 nm in *Trem2*$^{+/+}$, 396 nm in *Trem2*$^{+/-}$, and 442 nm in *Trem2*$^{-/-}$). This suggests that the microglia barrier prevents the radial extension of β-amyloid fibrils, promoting their intermingling and formation of mesh-like structures with various degrees of compaction. The longer amyloid fibers, coupled with their increased branching at the nano scale (Figure 4G), lead to a marked increase in fibril surface area in *Trem2* deficiency (see Supplemental Information).

Microglia Processes Envelop Individual Fibrils in Early Filamentous Plaques and Promote Their Compaction

To explore the role of microglia and *TREM2* deficiency in the earliest stages of amyloid deposition in mice, we obtained high-resolution confocal images of clusters of thioflavin S-positive fibrils that lacked a dense core, which we termed filamentous plaques (Figure 4A). Interestingly, we observed that these plaques were highly intermingled with microglia processes (Figure 4A). Processes that directly contacted thioflavin S-positive amyloid filaments were highly enriched in Trem2 (Figure 4B). These processes appeared to closely wrap around individual amyloid filaments as evidenced by the fact that the membrane-bound Trem2 was highly colocalized with the filaments, while the parent microglia branches filled with cytoplasmic Iba1 were immediately adjacent (Figure 4C). We also observed instances in which more mesh-like clusters of fibrils were fully wrapped by fine Trem2-positive microglia processes that appeared to cap individual fibril endings. (Figure 4D). This suggests that these early interactions between microglia processes and amyloid filaments could be of importance in determining the degree of fibril compaction.

To explore this possibility, we examined the nanostructures within diffuse fibrils revealed by super-resolution STORM imaging. Within individual plaques, we observed fibrils with variable widths ranging from 30 nm (about the resolution limit of our STORM imaging) to 160 nm (Figures 4E and 4F). Consistent with atomic-force microscopy data in vitro (Stine et al., 1996), this suggests that Aβ fibrils coil together to form bundle-like structures of different widths in vivo. Interestingly, *Trem2* deficiency led to an increased proportion of thin fibril bundles (~40 nm) and decreased proportion of thicker ones (average 68 nm in *Trem2*$^{+/+}$, 57 nm in *Trem2*$^{+/-}$, and 48 nm in *Trem2*$^{-/-}$) (Figure 4G). Furthermore, we observed branched structures extending orthogonally from the main Aβ fibril bundle (Figure 4H), which were markedly increased in plaques from *Trem2*-deficient mice (Figure 4I). Together, the increased numbers of diffuse thin fibers projecting outward for greater lengths and the increased

Figure 2. Defective Microglia Barrier but Normal Aβ Phagocytosis in *Trem2* or *DAP12* Haplodeficiency

(A) Confocal images of Iba1-immunostained microglia (white) around thioflavin S+ amyloid plaques (cyan) in *5XFAD* mice with different *Trem2* genotypes or in *APPPS1-21* mice with different *DAP12* genotypes. Cyan asterisks indicate locations of the plaque. Red arrows point to the polarized microglia processes.

(B) Quantification of microglia process polarization away from or near plaques in *5XFAD* mice with different *Trem2* genotypes. n = 3 mice for each group; 540 microglia analyzed. Two-way ANOVA with post hoc Tukey tests were used for statistical comparisons.

(C and D) Quantification of microglia plaque coverage ("barrier") around plaques in *5xFAD* mice with different *Trem2* genotypes (C) and *APPPS1-21* mice with different *DAP12* genotypes (D). n = 6 mice for each group, 2,887 plaques for *5XFAD:Trem2* and 598 plaques for *APPPS1-21:DAP12*.

(E) Microglia barrier (white) interdigitates with the surface of an amyloid plaque (cyan) in wild-type *5XFAD* mice. Dotted cyan and red lines indicate thresholded borders of plaque and microglia, respectively.

(F) Dysmorphic microglia processes (white) with looping structures (red arrows) in mice with Trem2 or DAP12 deficiency.

(G) Confocal images of Aβ immunolabeling (4G8) within microglial phagosomes (CD68^{+}; green) in *Trem2*$^{+/+}$ (left) and *Trem2*$^{-/-}$ (right) from *5xFAD* brain slices. Yellow arrows indicate colocalized 4G8^{+} Aβ (magenta) and CD68^{+} (green) vesicles.

(H) Quantification of CD68^{+} vesicle area and 4G8 fluorescence per microglia. n = 3 mice for each group and 321 cells. One-way ANOVA with post hoc Tukey tests were used for statistical comparisons within each size group in panels (C) and (D) and within CD68 or Aβ measurements in panel (H), $^{**}p < 0.01$, $^{***}p < 0.001$; n.s.: $p > 0.05$; a.u., arbitrary unit. Data presented as mean ± SEM. All analyses were performed with mouse somatosensory cortex.

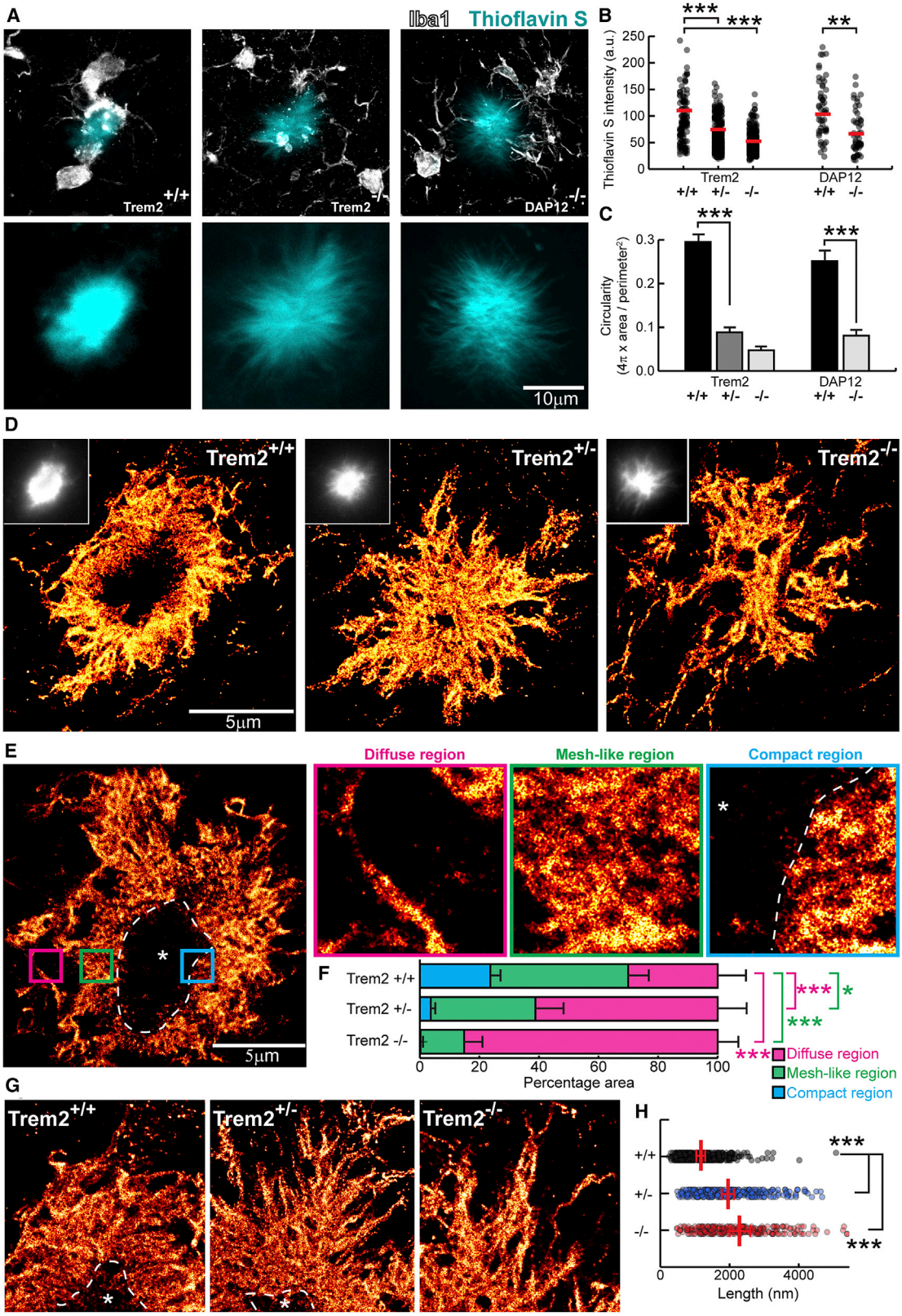

(legend on next page)

orthogonal branches, implies that the surface-to-volume ratio of amyloid fibers in *Trem2*-deficient mice is significantly greater than in wild-type mice (we estimate an ~300%–400% increase; see Supplemental Information). This phenomenon would be predicted to dramatically increase the contact area between amyloid fibrils and the adjacent exposed cellular structures. Importantly, while the total number of amyloid plaques was not significantly different between *Trem2*-deficient and wild-type mice (Figure 4J and Figure S3), we observed a significant increase in the proportion of filamentous plaques in both $Trem2^{+/-}$ and $Trem2^{-/-}$ mice (Figure 4J). The increase in filamentous plaques coupled with the greater surface area of individual plaques in $Trem2^{+/-}$ mice may lead to worsened neurotoxicity.

Decreased Amyloid Plaque Compaction in *Trem2* or *DAP12* Deficiency Leads to Severe Axonal Dystrophy

To directly test the degree of neurotoxicity, we measured the volume of axonal dystrophy around individual amyloid plaques using immunohistochemistry for Lamp1, a lysosomal protein highly enriched in dystrophic neurites (DN) that serves as a reliable marker for quantitative DN measurements (Condello et al., 2015, 2011; Gowrishankar et al., 2015). We classified plaques by morphology and size with specific attention to early filamentous plaques that were surprisingly associated with a massive amount of dystrophic neurites (Figures 5A and 5B). We found that *Trem2* or $DAP12^{+/-}$ and $DAP12^{-/-}$ mice had a much greater degree of axonal dystrophy than wild-type mice (Figures 5C and 5D). Interestingly, the main difference in dystrophy occurred in non-compact filamentous and small compact plaques (up to 6 μm in diameter), suggesting that the protective effect of microglia is most effective at early stages of plaque evolution. Given that filamentous plaques are associated with a surprisingly large degree of axonal dystrophy (Figure 5B), a shift of the distribution toward filamentous plaques could have critical effects on the overall degree of neural circuit disruption at early stages of amyloid accumulation.

TREM2 R47H Mutations Disrupt the Microglia Barrier Function in Late-Onset Human AD

To determine whether our findings in mice are relevant for human AD pathogenesis, we next characterized the microglia and plaque phenotypes in postmortem human brains from sporadic late onset AD cases and patients with R47H *TREM2* variant. Consistent with previous reports on late-onset AD, we observed different types of plaque morphologies using anti-Aβ immunolabeling (4G8) and thioflavin S (TS) staining (Figure 6A). We classified them into four categories: (1) diffuse plaques: diffuse 4G8+ fibrils lacking TS labeling; (2) filamentous plaques: 4G8+ halo and filamentous TS labeling with no plaque core; (3) compact plaques: 4G8+ halo and TS-labeled core; and (4) inert: TS-labeled core with no 4G8 halo. Interestingly, microglia processes did not display any polarization toward diffuse plaques but showed enlarged processes that robustly intermingled with both filamentous and compact plaques (Figures 6A and 6B). Moreover, plaques that had a TS-labeled core with no 4G8 halo had very few microglia processes (Figure 6A) or dystrophic neurites (Figure 7A) around them, which motivated us to call them inert.

We next quantified the relative proportions of these plaque categories in AD cases with and without the R47H *TREM2* mutation (Table S2). While we did not find a significant difference in the overall microglia density or amyloid plaque burden between genotypes (Figure S6), we did observe a robust increase in the proportion of plaques with filamentous morphology (Figure 6C). Remarkably, we observed a marked reduction in the number of surrounding microglia in both filamentous and compact plaques but we saw no significant microglia differences around diffuse and inert plaques (Figure 6C) or in non-plaque regions (Figure S6). Thus, the R47H mutation in humans leads to a specific defect of microglia plaque engagement, which is strikingly similar to the phenotype in *Trem2*- and *DAP12*-haplodeficient mice.

We then sought to determine how the observed decrease in microglia numbers in R47H mutants impacts their capacity for envelopment of individual filaments and plaque cores. Like in mice, we observed that microglia processes infiltrated filamentous plaques and had a tendency to surround individual filaments (Figure 6D). In contrast, microglia around compact plaques projected robust processes that closely enveloped the plaque surface (Figure 6E). Interestingly, while microglia in R47H mutants were able to send processes toward amyloid deposits, these appeared to be less robust and did not tightly engage with individual fibrils or the plaque surface, leading to a markedly diminished microglia coverage of amyloid aggregates (Figures 6F–6H). Thus, *TREM2* in humans likely regulates the

Figure 3. Super-resolution STORM Imaging Reveals a Marked Reduction in Plaque Compaction in *Trem2* Haplodeficiency

(A) Confocal images of thioflavin S-labeled amyloid plaques in $Trem2^{+/+}$ and $Trem2^{-/-}$ *5XFAD* mice and $DAP12^{-/-}$ *APPPS1-21* mice.

(B and C) Quantification of mean thioflavin S fluorescence intensity (B) and circularity (C, roundness) in plaques from *5XFAD* mice with different *Trem2* genotypes and *APPPS1-21* mice with different *DAP12* genotypes. n = 3 mice for each group, 747 plaques for *5XFAD:Trem2* and 198 plaques for *APPPS1-21:DAP12*.

(D and E) Immunolabeled Aβ plaque fibrils reconstructed by super-resolution STORM imaging. Images were pseudo-colored according to the reconstructed intensities. Insets in (D) show the same plaque imaged with wild-field illumination. Dashed line and asterisk in (E) indicate locations of the compact plaque core which is not labeled due to poor antibody penetration in *5XFAD* $Trem2^{+/+}$ mice (Figure S6). Three insets in (E) show high zoom examples of different types of Aβ fibril organization located in plaque regions with different degree of compaction.

(F) Quantification of the proportion of diffuse, mesh-like, and compact regions in amyloid plaques from *5XFAD* mice with different *Trem2* copy numbers. n = 8 plaques from each genotype. Two-way ANOVA with post hoc Tukey tests were used for statistical comparisons.

(G) Example images of fibrils within the diffuse plaque region extending radially from the plaque center in *5XFAD* mice with different *Trem2* genotypes. Dashed lines and asterisks indicate locations of the unlabeled compact plaque core.

(H) Quantification of lengths of the diffuse fibrils in plaques of *5XFAD* mice with different *Trem2* copy numbers. Scatterplot shows individual data point. Red bars indicate group averages by genotypes. Except for comparison in (F), Student's t tests were used for statistical comparisons in DAP12 groups in (B) and (C). One-way ANOVA with post hoc Tukey tests were used in Trem2 groups in (B) and (C), and in panel (H), $^{**}p < 0.01$, $^{***}p < 0.001$; a.u., arbitrary unit. Data presented as mean ± SEM.

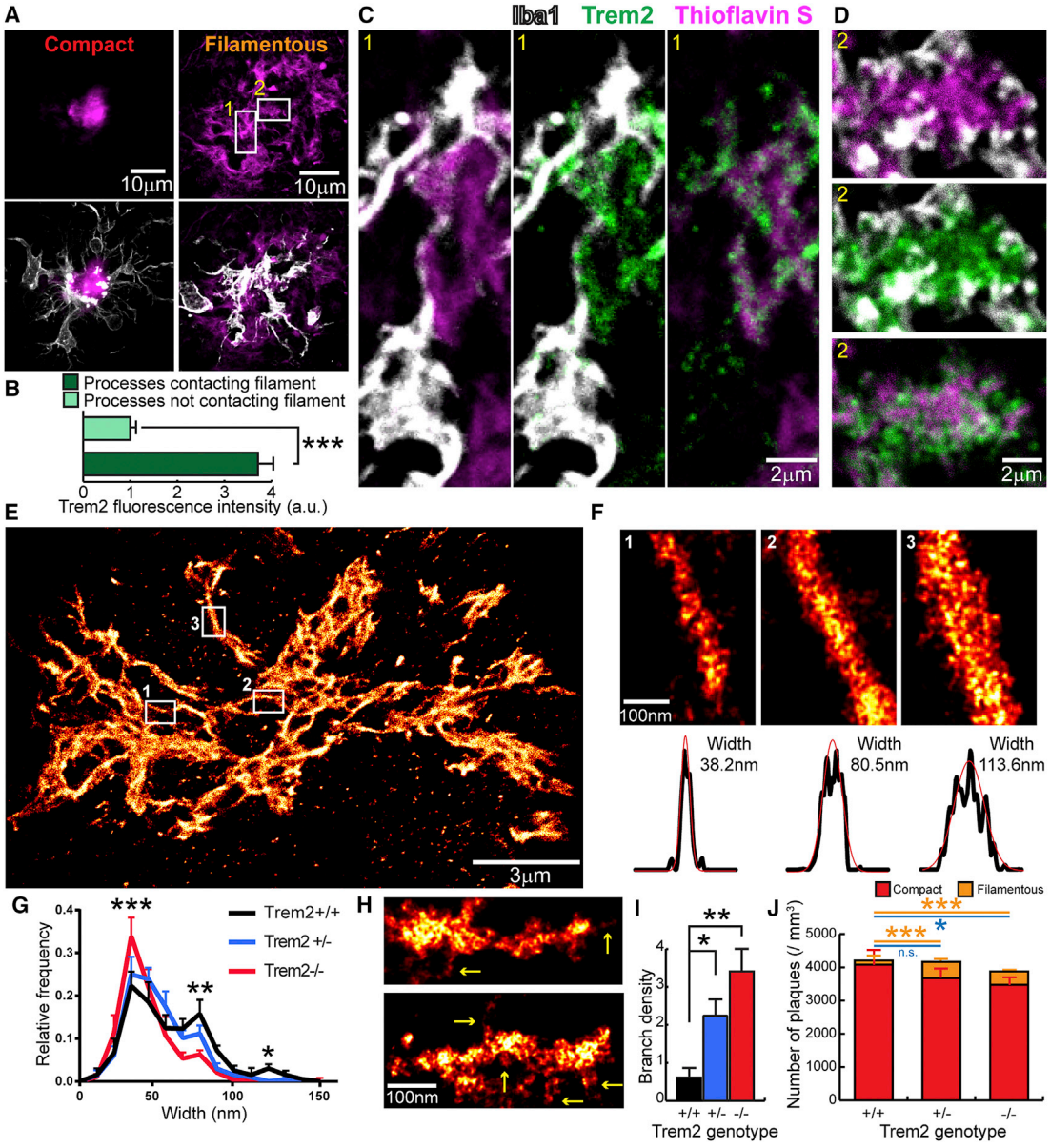

Figure 4. *Trem2* Deficiency Impairs Early-Stage Amyloid Fibril Envelopment by Microglia Leading to Increased Fibril Branching

(A) Confocal images of filamentous and compact plaques using thioflavin S labeling (magenta) in *5XFAD* mice showing close interaction with surrounding microglia (anti-Iba1 immunostaining, white).

(B) Quantification of Trem2 fluorescence intensity in microglia processes that do and do not contact with amyloid fibrils. n = 30 plaques, Student's t tests were used for statistical comparisons.

(C and D) Zoomed images from insets in (A), showing Trem2-enriched microglia processes wrapping around individual amyloid fibrils in a filamentous plaque.

(E and F) Examples of Aβ fibril nanostructures revealed by STORM imaging. Images were pseudo-colored according to the reconstructed intensities. Three insets in (E) show examples of individual fibrils. By fitting the cross-section fluorescence intensity to a Gaussian distribution, the widths of the fibril were derived as 2.35 times the SD of the fitted curve.

(G) Distribution of the Aβ fibril widths in plaques of *5XFAD* mice with different copy numbers of the *Trem2* gene. n = 8 plaques from each genotype, more than 200 fibrils were measured per plaque. Statistical comparisons between genotypes at various width sizes were calculated using two-way ANOVA with post hoc Tukey tests. Asterisks indicate statistical significance between Trem2 +/+ and −/−.

(H) Examples of individual Aβ fibril nanostructures branching orthogonally from the primary fiber bundle revealed by STORM imaging (yellow arrows).

(I) Quantification of the frequency of branched Aβ nanostructures per 500 nm in *5XFAD* mice with different copy numbers of the *Trem2* gene.

(J) Quantification of compact (thioflavin S^+ core with $4G8^+$ halo, red) and filamentous (diffuse filamentous thioflavin S labeling with $4G8^+$ halo, orange) plaque densities in *5XFAD* mice with different copy numbers of the Trem2 gene. Blue lines refer to statistical analyses for total plaques. n = 6 mice for each group; total 2,887 plaques analyzed. One-way ANOVA with post hoc Tukey tests were used for statistical comparisons in panel (I) and separately for filamentous and total plaques in panel (J), *p < 0.05, **p < 0.01, ***p < 0.001; a.u., arbitrary unit; n.s., p > 0.05.

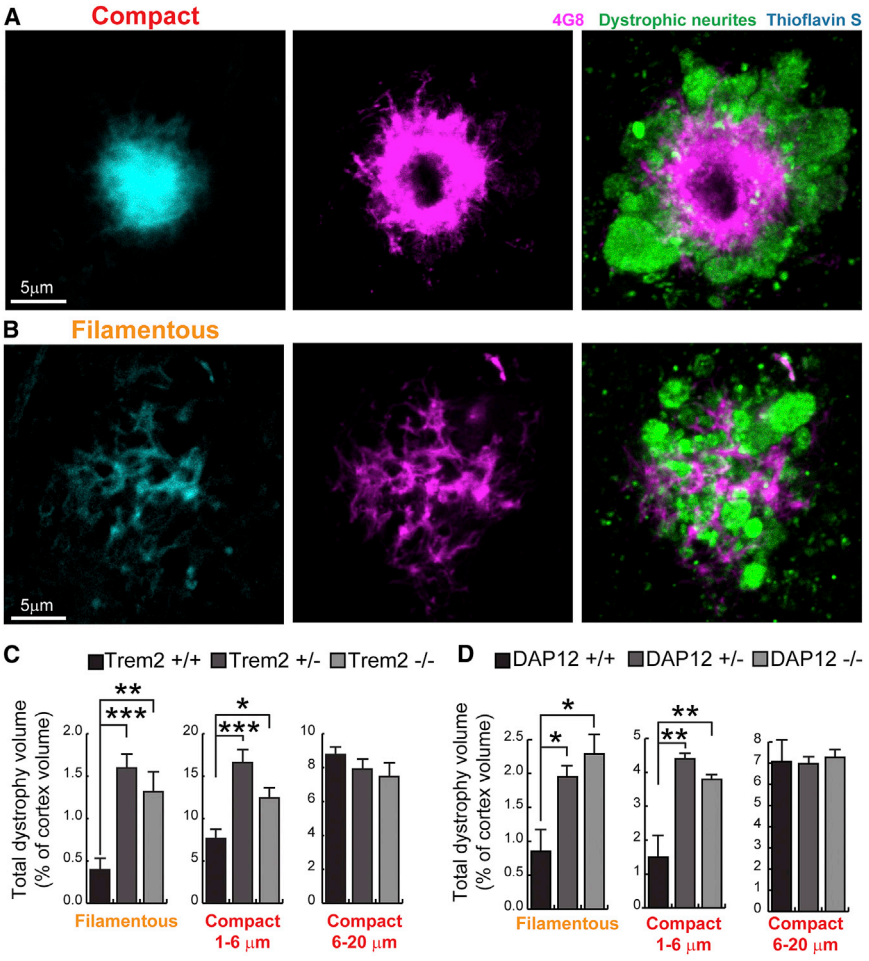

Figure 5. *Trem2* or *DAP12* Deficiency Leads to More Severe Plaque-Associated Axonal Dystrophy

(A and B) Visualization of Lamp1-immunolabeled axonal dystrophy (green) around compact (A) and filamentous (B) plaques in AD-like mouse brains. (C and D) Quantification of total dystrophy volume in cortex of AD-like mice with different *Trem2* (C) or *DAP12* (D) genotypes. n = 6 mice for each group of *5XFAD:Trem2* mice; total 2,887 plaques analyzed. n = 3 mice for each group of *APPPS1-21:DAP12* mice; total 1,076 plaques analyzed. One-way ANOVA with post hoc Tukey tests were used for all statistical comparisons, *p < 0.05, **p < 0.01, ***p < 0.001; a.u., arbitrary unit. Data presented as mean ± SEM. All analyses were performed with somatosensory cortex in mice.

microglia barrier function and disruption of this function in R47H mutants is associated with inability of microglia for enveloping fibrils or amyloid deposits.

Increased Tau Hyperphosphorylation and Axonal Dystrophy around Filamentous and Compact Plaques in Human R47H Mutants

To determine the consequences of a deficient microglia barrier in human AD with R47H *TREM2* variant, we quantified the extent of axonal dystrophy around individual plaques. Similar to mice, we found that filamentous plaques lacking a core had a surprisingly large number of dystrophic axons, as visualized by anti-APP immunohistochemistry (Figure 7A). Interestingly, we found a dramatic increase in axonal dystrophy around both filamentous and small compact plaques in R47H mutants compared to sporadic non mutant AD cases (Figure 7B).

These dystrophic swellings were associated with marked cytoskeletal abnormalities as evidenced by the extensive neuritic labeling with anti-phosphotau antibody around both filamentous and compact amyloid deposits (Figure 7C). Similar to our results quantifying APP-positive dystrophic neurites, phosphotau labeling was markedly increased in R47H AD brains compared to sporadic AD cases (Figure 7D). Consistent with our previous findings in mice (Condello et al., 2015) (Figure S1), we observed a strong anti-co-localization between microglia processes and hyperphosphorylated tau-positive dystrophic neurites (Figures 7E and 7F), suggesting that microglia normally exert a protective insulating effect. This function is disrupted in R47H mutants as demonstrated by a significantly reduced degree and robustness of microglia plaque coverage associated with increased neuritic abnormalities (Figure 7G).

DISCUSSION

Our study has uncovered previously unrecognized microglia functions that may participate in the pathogenesis of Alzheimer's disease. We examined microglia-plaque interactions in AD-like mice lacking *Trem2* and *DAP12* genes as well as in postmortem brains from human AD patients with R47H mutations. This enabled us to demonstrate that the tight envelopment of fibrils and early-stage plaques by microglia processes ("microglia barrier") may play a role in inducing amyloid fibril compaction and in reducing the surface area of potentially neurotoxic fibrils exposed to surrounding neural structures (Figure S7). This potentially neuroprotective microglial function provides a novel cellular mechanism that may explain the increased risk of Alzheimer's disease with *TREM2* genetic variants. It may also provide important insights for the more common forms of sporadic AD in which microglia senescence may drive similar functional deficits in barrier formation (Condello et al., 2015).

Microglia function in AD remains controversial with some evidence suggesting that they play a neurotoxic role by secreting reactive oxygen species and cytokines (Block et al., 2007). In advance neuropathological stages in mice, it has been shown that eliminating microglia with CSF1R antagonists leads to beneficial behavioral effects without changes in plaque numbers (Dagher et al., 2015; Olmos-Alonso et al., 2016), consistent with a toxic effect of microglia. In contrast, our results demonstrate a potentially neuroprotective role of microglia in early stages of plaque evolution, evidenced by the fact that areas covered by

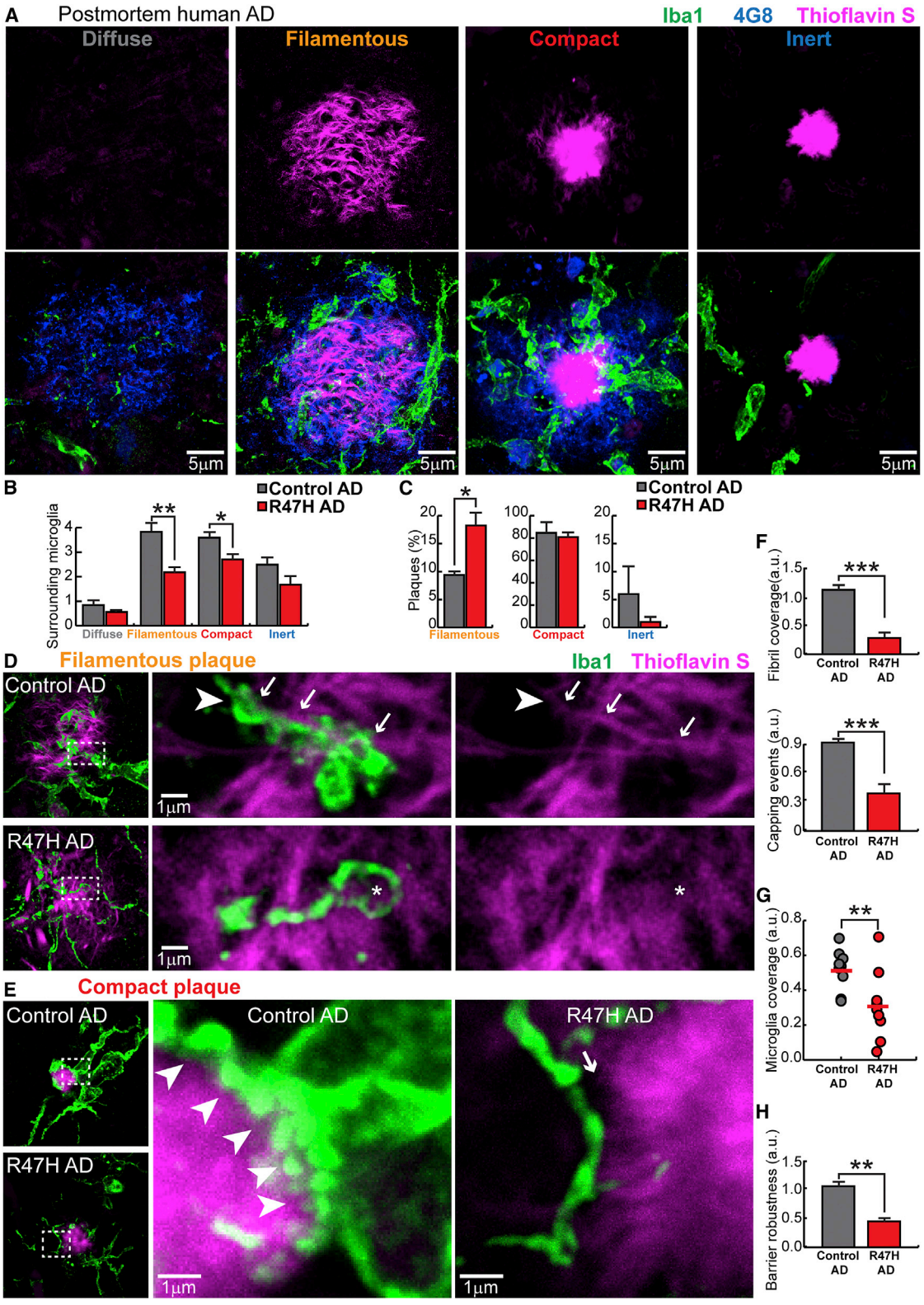

Figure 6. *TREM2* R47H Mutations in Human AD Lead to Abnormal Microglia Coverage around Filamentous and Compact Plaques

(A) Confocal images of thioflavin S-stained amyloid deposits (magenta), 4G8-labeled Aβ (blue), and Iba1-labeled surrounding microglia (green) in human postmortem AD brains, showing four different subtypes of plaques.

(legend continued on next page)

microglia processes develop fewer dystrophic neurites (Condello et al., 2015) and by the finding that inability of microglia to engage with plaques in R47H mutations is associated with increased axonal dystrophy in humans. Furthermore, we find it unlikely that microglia are actively involved in the formation or pruning of dystrophic axons given that we never find their processes directly surrounding or engulfing individual dystrophic neurites (Figure S7) (Condello et al., 2015).

While the function of *TREM2* in peripheral immune cell responses to pathogens has been extensively studied (Colonna, 2003), its role in AD remains poorly understood. Particularly, the precise mechanisms underlying the association between increased risk for AD and R47H *TREM2* variant is not known. The present study describes a novel role for *Trem2* in the polarization of microglial processes to envelope Aβ deposits and form a potentially neuroprotective barrier around them. *Trem2* or *DAP12* haplodeficiency in AD mice dramatically reduces plaque-associated microglia and disrupts the barrier formation. Strikingly, in humans with R47H mutations, we observed a nearly identical phenotype with a marked reduction in microglia coverage of filamentous and small compact plaques that was associated with more severe axonal dystrophy and hyper-phosphorylated tau in neurites.

Surprisingly, despite in vitro studies suggesting otherwise (Kleinberger et al., 2014), we found that Aβ phagocytosis by microglia in *Trem2* haplodeficiency appears to remain normal in vivo. This result suggests that rather than defective phagocytosis, disruption of the microglia barrier could be a driving mechanism underlying increased risk for AD with single allele *TREM2* mutations in humans. In contrast, when complete protein loss occurred in $Trem2^{-/-}$ mice, we did observe a significant reduction in phagocytosis (Figures 2G and 2H). Defective phagocytosis may be more relevant for explaining the much less common Nasu-Hakola disease in which homozygous *TREM2* mutations cause a multi-organ condition associated with aggressive neurodegeneration but with very different neuropathological features from AD (Paloneva et al., 2000).

Interestingly, while in *Trem2*- and *DAP12*-deficient mice as well as R47H human mutants, microglia processes are unable to form a robust barrier, they are still moderately polarized, sending fine processes toward plaques (Figures 2A and 2B). This suggests that separate molecular mechanisms (El Khoury et al., 2003; Reed-Geaghan et al., 2009; Song et al., 2011) mediate the chemotactic plaque attraction and projection of microglia processes versus the formation of a tight and robust envelopment of amyloid fibrils and deposits, which seems to be highly dependent on Trem2 signaling. Given the recent findings that Trem2 recognizes various types of lipids that are present in amyloid plaques (Wang et al., 2015), we postulate that the extent and types of lipids decorating the plaque surface may regulate the microglia barrier through Trem2 signaling. Consistent with this hypothesis, microglia around diffuse plaques do not have a very activated and polarized morphology (Figure 6), and spectrochemical analysis shows that diffuse plaques do not have prominent lipid coating on their surface (Liao et al., 2013; Rak et al., 2007). In contrast, as amyloid deposits become filamentous and thioflavin S positive, which likely makes them more lipophilic (Hilbich et al., 1992), they robustly attract microglia processes, consistent with recent in vivo imaging studies (Jung et al., 2015). It is therefore conceivable that conditions affecting brain lipid metabolism, such as *ApoE* genetic polymorphisms (Kim et al., 2009) or other mechanisms that alter brain lipids (Dietschy and Turley, 2004), may affect amyloid pathology by differentially modulating the formation of a microglia barrier.

Loss of microglia barrier function leads to decreased Aβ fibril compaction as evidenced by our direct visualization of amyloid plaque architecture with super-resolution STORM imaging (Figures 3 and 4) and the observed reduced thioflavin S fluorescence intensity (Figure 3). STORM imaging revealed that plaques in $Trem2^{+/+}$ mice have a more compact organization with more mesh-like structures and fibrils exhibiting greater widths and shorter lengths than those in $Trem2^{+/-}$ and $Trem2^{-/-}$ mice. It also showed that in Trem2 deficiency, fibrils have more nanoscale orthogonal branches originating from the primary bundle (Figures 3H and 3I). This is consistent with our previous observations that plaque regions not covered by microglia processes have a markedly higher density of Aβ protofibrils than covered regions (Condello et al., 2015).

The absolute widths measured by STORM imaging likely do not reflect the precise physical dimensions of single Aβ fibrils, given resolution limits (~30 nm) and the fact that antibody labeling itself changes the size of the imaged object. Interestingly, however, the range of different widths that we observed demonstrate three main size peaks (~40 nm, 80 nm, and 120 nm), suggesting that STORM might be capable of differentiating unitary Aβ fibrils (with attached primary and secondary antibodies) coiling together into larger bundles, consistent with in vitro studies using atomic-force microscopy (Stine et al., 1996). Together, these structural differences resulting from the lack of a microglia

(B) Quantification of the number of microglia within a 25 μm radius from the plaque perimeter for each plaque subtype in AD brains with and without *TREM2* R47H mutation. Total 1,966 plaques analyzed.

(C) Quantification of the proportion of plaque subtypes that demonstrated robust microglia interactions (diffuse plaques do not attract microglia processes and were excluded in this analysis) in AD brains with and without *TREM2* R47H mutation. Total 1,474 plaques analyzed.

(D and E) Confocal images of microglia coverage of individual amyloid filaments (D) and the surface of compact plaques (E). Right panels show zoomed images from dashed boxes on the left panels. Arrows indicate microglia processes closely wrapping around an amyloid fibril with a "capping" structure (arrow head). Asterisk shows a dysmorphic loop structure formed by microglia in AD brains with *TREM2* R47H mutation. In (E), white arrow heads outline the robust microglia coverage of the plaque surface. Arrow points to the gap between a dysmorphic microglia process and the plaque border in R47H mutant.

(F) Quantification of the amyloid filaments wrapped by microglia and the capping events in individual filamentous plaques. Total 226 plaques analyzed.

(G and H) Quantification of compact plaque surface coverage (G) and barrier robustness (H) (see Figure S7) by microglia in AD with and without R47H mutations. Total 1,157 plaques analyzed. For all quantifications, n = 9 control AD patients and n = 10 R47H AD patients. Student's t tests were used for all statistical comparisons with Bonferroni correction for multiple comparison in panels (B) and (C), $^{*}p < 0.05$, $^{**}p < 0.01$, $^{***}p < 0.001$; a.u., arbitrary unit. Data presented as mean ± SEM. All analyses were performed on plaques from middle frontal gyrus.

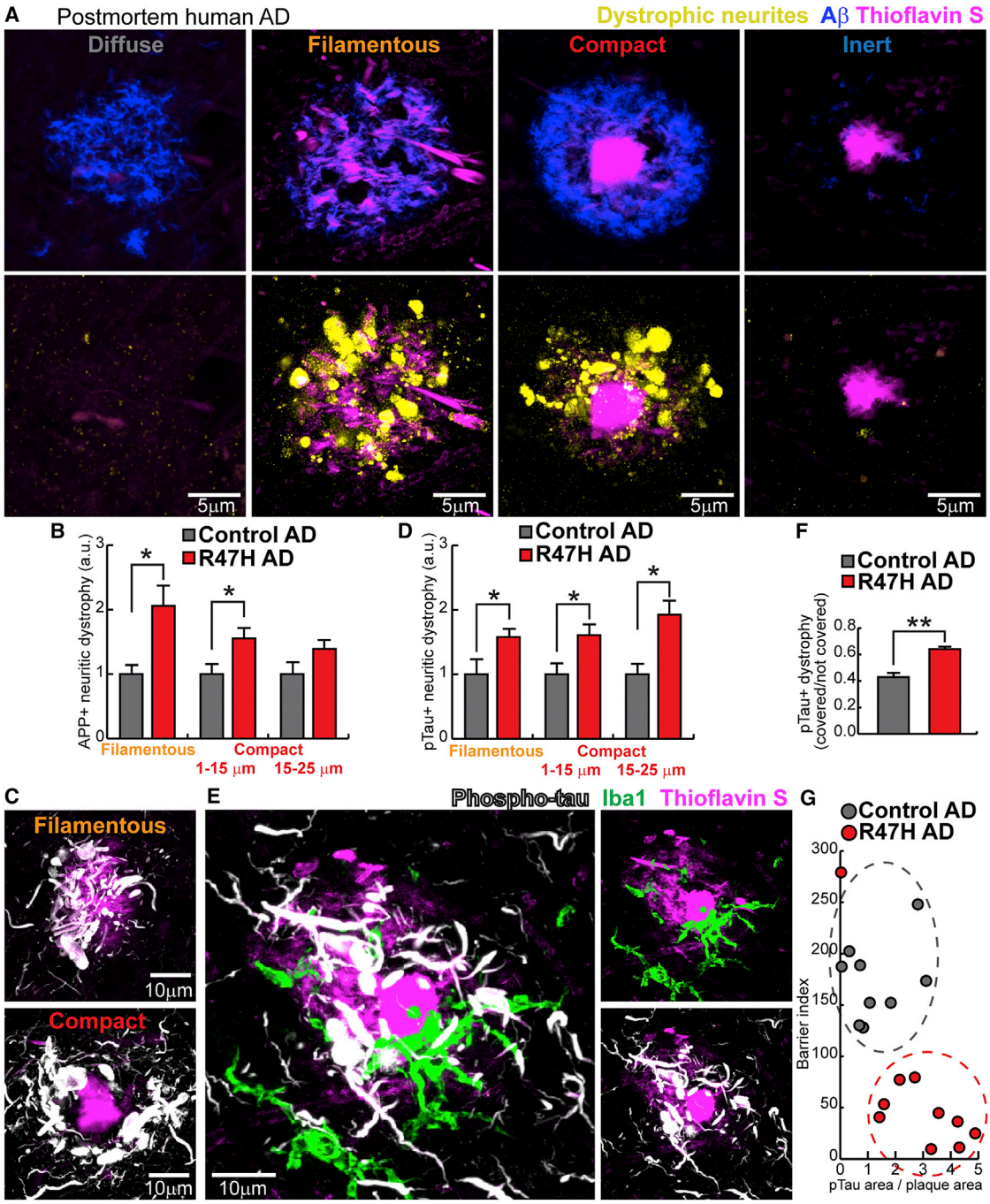

Figure 7. R47H Mutation in Humans Is Associated with Severe Neuritic Tau Hyperphosphorylation and Axonal Dystrophy

(A) Four subtypes of plaques in human brain. Diffuse plaques (anti $A\beta^+$, thioflavin S^-); filamentous plaques (anti $A\beta^+$, filamentous thioflavin S^+); compact plaques (anti $A\beta^+$, thioflavin S^+ compact core); inert plaques (anti $A\beta^-$, thioflavin S^+ compact core). Bottom: images of dystrophic neurites (labeled by anti-APP immunolabeling, yellow) around different subtypes of amyloid plaques in postmortem human brains. Notice the marked degree of dystrophy within the otherwise inconspicuous filamentous plaques.

(B) Quantification of APP^+ dystrophic neurites around individual plaques in AD patients with and without R47H mutations. Total 1,406 plaques analyzed.

(C) Confocal images of neurites with hyper-phosphorylated tau (white) around filamentous and compact plaques (magenta). Notice the marked degree of hyperphosphorylation in filamentous plaques.

(D) Quantification of area neurites with phosphorylated tau around individual plaques in AD patients with and without R47H mutations. Total 1,369 plaques analyzed.

(E) Microglia (green) in close contact with a plaque (magenta) but anti-colocalized with hyper-phosphorylated dystrophic neurites (white).

(legend continued on next page)

barrier are predicted to dramatically increase the surface area of an individual plaque (Supplemental Information). Differences in the degree of plaque compaction and fibril surface area may be key factors determining the degree of plaque neurotoxicity. Plaque regions not covered by microglia processes have lower degree of amyloid compaction but greater affinity for soluble Aβ42 (Figure S1) and form hotspots of potentially neurotoxic protofibrillar Aβ42 (Condello et al., 2015). Higher protofibrillar Aβ42, together with an overall increased contact area with surrounding neurites in *TREM2* deficiency, could synergistically contribute to the increased plaque neurotoxicity that we observed.

One intriguing aspect of our data is that the total number of thioflavin S compact plaques was modestly reduced in *Trem2*-deficient mice, while filamentous amyloid plaques without a compact core increased significantly. This is consistent with our model suggesting that the microglia barrier increases plaque compaction and failure of the barrier, such as in *Trem2* deficiency, shifts the balance of plaques toward a more diffuse phenotype without significantly altering total plaque number. This finding, which is dependent on the type of labels used for amyloid plaque quantification, may partly explain the initial contradicting results reported with regards to plaque density in *Trem2* deficiency (Jay et al., 2015; Wang et al., 2015).

Our surprising observation that small filamentous plaques cause a marked degree of axonal dystrophy around them in both mice and humans (Figures 5B and 7A) is consistent with the idea that less compact fibrils are more toxic than the compact ones in the plaque core. Thus, the observed shift toward a less compact plaque phenotype, coupled with the greater numbers of filamentous plaques, could significantly increase the overall degree of neural circuit damage despite a stable number of total plaques. Interestingly, our finding that diffuse plaques do not cause axonal dystrophy suggest that the transition from diffuse to β sheet-rich filamentous conformation (evidenced by thioflavin S labeling) is the critical neurotoxic event that leads to dystrophy consistent with recent in vivo imaging data (Bittner et al., 2012). While filamentous plaques represent a modest proportion of all plaques in AD-like mice (Figure 4J), we found them to be more prevalent in human sporadic AD brains (Figure 6C), which is likely due to the fact that plaque growth is protracted over decades compared to months in mice (Burgold et al., 2014; Condello et al., 2011). In addition, a plaque phenotype we called inert, because its core was intensely labeled by thioflavin S but was virtually devoid of dystrophic neurites, suggests that highly compact plaques may be minimally neurotoxic. These findings urge caution against using positron emission tomography (PET) amyloid tracers with predominant affinity to dense plaques and could partly explain the modest predictive value of current PET tracers such as PIB (Kepe et al., 2013) and the weak correlation between plaque load and cognitive dysfunction in postmortem studies (Morris et al., 2014).

Our data show that loss of the microglia barrier in mice with *Trem2* deficiency has the greatest impact on axonal dystrophy in filamentous and small compact plaques, but as plaques get bigger the difference in the degree of axonal dystrophy diminishes (Figure 5). A similar effect restricted to small plaques was previously observed when we enhanced the protective effects of the microglia barrier by genetic deletion of the chemokine receptor *CX3CR1* in mice (Condello et al., 2015). We hypothesize that the reason for this phenomenon is that in mice, the relatively rapid plaque growth may overwhelm the overall capacity of microglia neuroprotection and eventually most axons in their vicinity will be affected, thus causing the degree of measurable axonal dystrophy to plateau in large plaques. In human AD, we found that the effect of R47H mutations on the degree of axonal dystrophy was present over a broader range of plaque sizes than in mice (Figure 7). This is likely due to the fact that plaques are likely to grow much slower in humans. Thus, it is conceivable that the neuroprotective role of the microglia barrier in humans could be effective over more protracted time intervals than in transgenic mice.

While our study provides novel cellular phenomenology potentially relevant for understanding microglia function in both mice and humans, there remain uncertainties as to how the observed defective microglia barrier acts, at a more functional level, to cause pathological defects. Furthermore, while our findings demonstrate marked neuritic changes around plaques in *TREM2* deficiency, the relative functional contribution of dystrophic neurites compared to other pathologies such as synaptic loss, cell death and neurofibrillary tangles is unclear. Thus, the overall relevance of the microglia barrier function in the context of such complex neurodegenerative disorder remains to be determined.

Nevertheless, our results suggest that boosting the microglia barrier function or increasing plaque compactness by other means could constitute a novel strategy for AD therapeutics. Given the recent findings that *APOE* and *CD33* (whose genetic variants are common risk factors for AD) interact with the *TREM2* pathway (Atagi et al., 2015; Chan et al., 2015), our findings could have implications for the more prevalent forms of AD in which no mutations have been identified. Our current understanding of the cellular, molecular, and biophysical mechanisms by which microglia exert this potentially neuroprotective barrier function is limited. However, future studies elucidating such mechanisms may uncover targetable pathways that could specifically enhance the barrier function in microglia and reduce risk for AD.

EXPERIMENTAL PROCEDURES

Animals

All animal procedures were approved by the Institutional Animal Care and Use Committee at Yale, Weill Cornell College of Medicine and Washington

(F) Quantification of the degree of neuritic tau hyper-phosphorylation as a ratio between areas covered and not covered by microglia processes. Total 468 plaques analyzed.

(G) Quantification of the degree of microglia barrier (radial coverage multiply robustness; see Experimental Procedures) as a function of the degree of phosphorylated tau (normalized for plaque size). Total 1,008 plaques analyzed. For all quantifications, n = 9 control humans and n = 10 R47H humans. Student's t tests were used for all statistical comparisons with Bonferroni correction for multiple comparison in panels (B) and (D), *p < 0.05, **p < 0.01; a.u., arbitrary unit. Data presented as mean ± SEM. All analyses were performed on plaques from middle frontal gyrus.

University. *5XFAD* mice (Oakley et al., 2006) were cross-bred with *Trem2* knockout mice (Ulrich et al., 2014) as previously described (Wang et al., 2015). *APPPS1-21* (Radde et al., 2006) mice were cross-bred with *DAP12* knockout mice to obtain *DAP12*-deficient mice (Bakker et al., 2000). Unless specifically indicated, 4-month-old mice were used. *CRND8* mice (courtesy of Dr. David Westaway, University of Alberta) were also used.

Human Postmortem Brain Tissue

Formalin-fixed human postmortem brain tissue blocks were acquired from various brain banks. Detailed demographic and clinical information can be found in Table S2, including ten AD cases with the R47H mutation (Birdsill et al., 2011; Korvatska et al., 2015) and nine cases with comparable AD pathology but not carrying the mutation. Cases were matched for age, gender, and *ApoE* genotype.

Immunohistochemistry

Brain slices were obtained from the mouse posterior somatosensory cortex and human middle frontal gyrus. Mouse coronal sections were cut (40 μm thick) with a cryostat and human tissue was sectioned with a vibratome. Primary antibodies incubation were 2 days at 4°(PBS with 0.2% Triton X-100 and 5% goat serum) and secondary antibodies for 6 hr, before mounting on slides with PermaFluor (Thermo Scientific, TA-030-FM). Heat-induced sodium citrate antigen retrieval was performed for TREM2, DAP12, and all human tissue staining with the following protocol: tissue was boiled in 50 mM sodium citrate with 0.05% tween-20 at 95° for 45 min and then washed with PBS. The complete list of antibodies and reagents used in this study is included in the Supplemental Experimental Procedures.

Confocal Microscopy

A Leica SP5 confocal microscope was used to generate all images. Laser and detector (the GaAsP hybrid detection system, photon counting mode) settings were maintained constant. For all analyses, tiled imaging using a motorized stage was used to image across one cerebral hemisphere in mice. A 3 mm^2 human brain region per brain slice was imaged using a 63× oil immersion objective (N.A. 1.4) at 1,024 × 10,24 pixel resolution, z-step size of 3 μm, and identity was blinded for analyses (Yuan and Grutzendler, 2016). Images were processed with FIJI (ImageJ) software. A customized macro was used to segment individual amyloid plaque. The number of plaques analyzed ranged from 150 to 300 in each brain (see Supplemental Experimental Procedures).

STORM Imaging

Samples were mounted in a buffer consisting of 90% glycerol and 10% 10× PBS with an overall concentration of 10 mM cysteamine and 50 mM sodium sulfite (J.T. Baker 3922-01). Images were recorded on a modified Nikon Ti-E inverted microscope using a 60× 1.49 N.A. oil-immersion objective using an EMCCD camera (Andor IXon Ultra DU-897U-CS0-#BV). The objective was mounted on a custom mount to suppress thermal and mechanical drift and focusing was provided by a piezoelectric objective positioner (Physik Instrumente P-725.4CA). For illumination, a 642 nm solid-state laser (Omicron Lux, 20 kW/cm^2 at the sample) was used with a dichroic (Semrock, Di02-R635-25x36) and a band-pass filter (Semrock, BLP01-647R-25) for separation of excitation and emission. Field of view was selected using metal halide lamp (Prior Lumen 200) illumination before switching to laser illumination and was then imaged for approximately 20,000 frames using an exposure time of 25 ms and an EM-multiplication setting corresponding to a gain of 35.5. Events were detected and localized (Baddeley et al., 2009) and reconstructions were rendered using jittered triangulation (Baddeley et al., 2010) (see Supplemental Experimental Procedures).

Statistics

Data represented as mean ± SEM. Two-tail unpaired Student's t tests were employed for comparisons between two groups. p values in cases of multiple t-tests were corrected with Bonferroni method. One-way and two-way ANOVA tests were used for multiple group comparions with post hoc Tukey tests. A probability of $p < 0.05$ was considered indicative of significant differences between groups.

SUPPLEMENTAL INFORMATION

Supplemental Information includes Supplemental Experimental Procedures, seven figures, and two tables and can be found with this article online at http://dx.doi.org/10.1016/j.neuron.2016.05.003.

AUTHOR CONTRIBUTIONS

P.Y., C.C., and J.G. designed the study. P.Y. and C.C. performed experiments. D.B. and P.Y. performed STORM microscopy and analyzed the images. P.Y., C.C., and J.G. analyzed data. P.Y., C.C., and J.G. prepared the manuscript. C.D.K., T.D.B., S.M.P., W.L., Y.W., and M.C. provided critical reagents. J.G. supervised the study.

ACKNOWLEDGMENTS

We thank Lingling Ji (Yale University) for consultation on statistics and Katie N. Murray (Yale University) for critical reading of the manuscript. We thank the University of Washington Alzheimer's Disease Research Center Neuropathology Core for provision of human brain tissues (supported by NIA P50 AG05136). We thank Sun Health Research Institute Brain and Body Donation Program of Sun City, Arizona for the provision of human brain tissues, supported by the NINDS (U24 NS072026), the NIA (P30 AG19610), the Arizona Department of Health Services (contract 211002), and the Arizona Biomedical Research Commission (contracts 4001, 0011, 05-901 and 1001). We thank Dennis W. Dickson and Michael Deture at Mayo Clinic (Jacksonville, Florida) for providing additional human brain tissues. We thank the Helen and Robert Appel Alzheimer's Disease Research Institute for providing funding; Xiaoyu Hu for providing *DAP12* knockout mice; and Mathias Jucker for providing *APPPS1-21* mice. This project was supported by R01HL106815 and R21AG048181 (J.G.). This project was supported by National Institute of Health grants R01HL106815 and R21AG048181 (J.G.), and Alzheimer's Association Research Grant (J.G.).

Received: October 18, 2015
Revised: February 21, 2016
Accepted: April 17, 2016
Published: May 18, 2016; corrected online September 19, 2016

REFERENCES

Atagi, Y., Liu, C.-C., Painter, M.M., Chen, X.-F., Verbeeck, C., Zheng, H., Li, X., Rademakers, R., Kang, S.S., Xu, H., et al. (2015). Apolipoprotein E Is a Ligand for Triggering Receptor Expressed on Myeloid Cells 2 (TREM2). J. Biol. Chem. *290*, 26043–26050.

Baddeley, D., Jayasinghe, I.D., Cremer, C., Cannell, M.B., and Soeller, C. (2009). Light-induced dark states of organic fluochromes enable 30 nm resolution imaging in standard media. Biophys. J. *96*, L22–L24, http://dx.doi.org/10.1016/j.bpj.2008.11.002.

Baddeley, D., Cannell, M.B., and Soeller, C. (2010). Visualization of localization microscopy data. Microsc. Microanal. *16*, 64–72, http://dx.doi.org/10.1017/S143192760999122X.

Bakker, A.B., Hoek, R.M., Cerwenka, A., Blom, B., Lucian, L., McNeil, T., Murray, R., Phillips, L.H., Sedgwick, J.D., and Lanier, L.L. (2000). DAP12-deficient mice fail to develop autoimmunity due to impaired antigen priming. Immunity *13*, 345–353.

Birdsill, A.C., Walker, D.G., Lue, L., Sue, L.I., and Beach, T.G. (2011). Postmortem interval effect on RNA and gene expression in human brain tissue. Cell Tissue Bank. *12*, 311–318.

Bittner, T., Burgold, S., Dorostkar, M.M., Fuhrmann, M., Wegenast-Braun, B.M., Schmidt, B., Kretzschmar, H., and Herms, J. (2012). Amyloid plaque formation precedes dendritic spine loss. Acta Neuropathol. *124*, 797–807.

Block, M.L., Zecca, L., and Hong, J.-S. (2007). Microglia-mediated neurotoxicity: uncovering the molecular mechanisms. Nat. Rev. Neurosci. *8*, 57–69.

Burgold, S., Filser, S., Dorostkar, M.M., Schmidt, B., and Herms, J. (2014). In vivo imaging reveals sigmoidal growth kinetic of β-amyloid plaques. Acta Neuropathol. Commun. *2*, 30.

Chan, G., White, C.C., Winn, P.A., Cimpean, M., Replogle, J.M., Glick, L.R., Cuerdon, N.E., Ryan, K.J., Johnson, K.A., Schneider, J.A., et al. (2015). CD33 modulates TREM2: convergence of Alzheimer loci. Nat. Neurosci. *18*, 1556–1558.

Colonna, M. (2003). TREMs in the immune system and beyond. Nat. Rev. Immunol. *3*, 445–453.

Condello, C., Schain, A., and Grutzendler, J. (2011). Multicolor time-stamp reveals the dynamics and toxicity of amyloid deposition. Sci. Rep. *1*, 19.

Condello, C., Yuan, P., Schain, A., and Grutzendler, J. (2015). Microglia constitute a barrier that prevents neurotoxic protofibrillar Aβ42 hotspots around plaques. Nat. Commun. *6*, 6176.

Dagher, N.N., Najafi, A.R., Kayala, K.M.N., Elmore, M.R.P., White, T.E., Medeiros, R., West, B.L., and Green, K.N. (2015). Colony-stimulating factor 1 receptor inhibition prevents microglial plaque association and improves cognition in 3xTg-AD mice. J. Neuroinflammation *12*, 139.

Davalos, D., Grutzendler, J., Yang, G., Kim, J.V., Zuo, Y., Jung, S., Littman, D.R., Dustin, M.L., and Gan, W.-B.B. (2005). ATP mediates rapid microglial response to local brain injury in vivo. Nat. Neurosci. *8*, 752–758.

Dietschy, J.M., and Turley, S.D. (2004). Thematic review series: brain Lipids. Cholesterol metabolism in the central nervous system during early development and in the mature animal. J. Lipid Res. *45*, 1375–1397.

El Khoury, J.B., Moore, K.J., Means, T.K., Leung, J., Terada, K., Toft, M., Freeman, M.W., and Luster, A.D. (2003). CD36 mediates the innate host response to beta-amyloid. J. Exp. Med. *197*, 1657–1666.

Frank, S., Burbach, G.J., Bonin, M., Walter, M., Streit, W., Bechmann, I., and Deller, T. (2008). TREM2 is upregulated in amyloid plaque-associated microglia in aged APP23 transgenic mice. Glia *56*, 1438–1447.

Gowrishankar, S., Yuan, P., Wu, Y., Schrag, M., Paradise, S., Grutzendler, J., De Camilli, P., and Ferguson, S.M. (2015). Massive accumulation of luminal protease-deficient axonal lysosomes at Alzheimer's disease amyloid plaques. Proc. Natl. Acad. Sci. USA *112*, E3699–E3708.

Guerreiro, R., Wojtas, A., Bras, J., Carrasquillo, M., Rogaeva, E., Majounie, E., Cruchaga, C., Sassi, C., Kauwe, J.S.K., Younkin, S., et al.; Alzheimer Genetic Analysis Group (2013). TREM2 variants in Alzheimer's disease. N. Engl. J. Med. *368*, 117–127.

Hanisch, U.-K.K., and Kettenmann, H. (2007). Microglia: active sensor and versatile effector cells in the normal and pathologic brain. Nat. Neurosci. *10*, 1387–1394.

Hilbich, C., Kisters-Woike, B., Reed, J., Masters, C.L., and Beyreuther, K. (1992). Substitutions of hydrophobic amino acids reduce the amyloidogenicity of Alzheimer's disease beta A4 peptides. J. Mol. Biol. *228*, 460–473.

Jay, T.R., Miller, C.M., Cheng, P.J., Graham, L.C., Bemiller, S., Broihier, M.L., Xu, G., Margevicius, D., Karlo, J.C., Sousa, G.L., et al. (2015). TREM2 deficiency eliminates TREM2+ inflammatory macrophages and ameliorates pathology in Alzheimer's disease mouse models. J. Exp. Med. *212*, 287–295.

Jin, S.C., Benitez, B.A., Karch, C.M., Cooper, B., Skorupa, T., Carrell, D., Norton, J.B., Hsu, S., Harari, O., Cai, Y., et al. (2014). Coding variants in TREM2 increase risk for Alzheimer's disease. Hum. Mol. Genet. *23*, 5838–5846.

Jonsson, T., Stefansson, H., Steinberg, S., Jonsdottir, I., Jonsson, P.V., Snaedal, J., Bjornsson, S., Huttenlocher, J., Levey, A.I., Lah, J.J., et al. (2013). Variant of TREM2 associated with the risk of Alzheimer's disease. N. Engl. J. Med. *368*, 107–116.

Jung, C.K.E., Keppler, K., Steinbach, S., Blazquez-Llorca, L., and Herms, J. (2015). Fibrillar amyloid plaque formation precedes microglial activation. PLoS ONE *10*, e0119768.

Kepe, V., Moghbel, M.C., Långström, B., Zaidi, H., Vinters, H.V., Huang, S.-C., Satyamurthy, N., Doudet, D., Mishani, E., Cohen, R.M., et al. (2013). Amyloid-β positron emission tomography imaging probes: a critical review. J. Alzheimers Dis. *36*, 613–631, http://dx.doi.org/10.3233/JAD-130485.

Kim, J., Basak, J.M., and Holtzman, D.M. (2009). The role of apolipoprotein E in Alzheimer's disease. Neuron *63*, 287–303.

Kleinberger, G., Yamanishi, Y., Suárez-Calvet, M., Czirr, E., Lohmann, E., Cuyvers, E., Struyfs, H., Pettkus, N., Wenninger-Weinzierl, A., Mazaheri, F., et al. (2014). TREM2 mutations implicated in neurodegeneration impair cell surface transport and phagocytosis. Sci. Transl. Med. *6*, 243ra86.

Korvatska, O., Leverenz, J.B., Jayadev, S., McMillan, P., Kurtz, I., Guo, X., Rumbaugh, M., Matsushita, M., Girirajan, S., Dorschner, M.O., et al. (2015). R47H Variant of TREM2 Associated With Alzheimer Disease in a Large Late-Onset Family: Clinical, Genetic, and Neuropathological Study. JAMA Neurol. *72*, 920–927.

Lee, C.Y.D., and Landreth, G.E. (2010). The role of microglia in amyloid clearance from the AD brain. J Neural Transm (Vienna) *117*, 949–960.

Liao, C.R., Rak, M., Lund, J., Unger, M., Platt, E., Albensi, B.C., Hirschmugl, C.J., and Gough, K.M. (2013). Synchrotron FTIR reveals lipid around and within amyloid plaques in transgenic mice and Alzheimer's disease brain. Analyst (Lond.) *138*, 3991–3997.

Liu, Z., Condello, C., Schain, A., Harb, R., and Grutzendler, J. (2010). CX3CR1 in microglia regulates brain amyloid deposition through selective protofibrillar amyloid-β phagocytosis. J. Neurosci. *30*, 17091–17101.

Lue, L.-F., Schmitz, C.T., Serrano, G., Sue, L.I., Beach, T.G., and Walker, D.G. (2015). TREM2 Protein Expression Changes Correlate with Alzheimer's Disease Neurodegenerative Pathologies in Post-Mortem Temporal Cortices. Brain Pathol. *25*, 469–480.

Matarin, M., Salih, D.A., Yasvoina, M., Cummings, D.M., Guelfi, S., Liu, W., Nahaboo Solim, M.A., Moens, T.G., Paublete, R.M., Ali, S.S., et al. (2015). A genome-wide gene-expression analysis and database in transgenic mice during development of amyloid or tau pathology. Cell Rep. *10*, 633–644.

Morris, G.P., Clark, I.A., and Vissel, B. (2014). Inconsistencies and controversies surrounding the amyloid hypothesis of Alzheimer's disease. Acta Neuropathol. Commun. *2*, 135.

Oakley, H., Cole, S.L., Logan, S., Maus, E., Shao, P., Craft, J., Guillozet-Bongaarts, A., Ohno, M., Disterhoft, J., Van Eldik, L., et al. (2006). Intraneuronal beta-amyloid aggregates, neurodegeneration, and neuron loss in transgenic mice with five familial Alzheimer's disease mutations: potential factors in amyloid plaque formation. J. Neurosci. *26*, 10129–10140.

Olmos-Alonso, A., Schetters, S.T.T., Sri, S., Askew, K., Mancuso, R., Vargas-Caballero, M., Holscher, C., Perry, V.H., and Gomez-Nicola, D. (2016). Pharmacological targeting of CSF1R inhibits microglial proliferation and prevents the progression of Alzheimer's-like pathology. Brain *139*, 891–907.

Paloneva, J., Kestilä, M., Wu, J., Salminen, A., Böhling, T., Ruotsalainen, V., Hakola, P., Bakker, A.B., Phillips, J.H., Pekkarinen, P., et al. (2000). Loss-of-function mutations in TYROBP (DAP12) result in a presenile dementia with bone cysts. Nat. Genet. *25*, 357–361.

Peng, Q., Malhotra, S., Torchia, J.A., Kerr, W.G., Coggeshall, K.M., and Humphrey, M.B. (2010). TREM2- and DAP12-dependent activation of PI3K requires DAP10 and is inhibited by SHIP1. Sci. Signal. *3*, ra38.

Radde, R., Bolmont, T., Kaeser, S.A., Coomaraswamy, J., Lindau, D., Stoltze, L., Calhoun, M.E., Jäggi, F., Wolburg, H., Gengler, S., et al. (2006). Abeta42-driven cerebral amyloidosis in transgenic mice reveals early and robust pathology. EMBO Rep. *7*, 940–946.

Rak, M., Del Bigio, M.R., Mai, S., Westaway, D., and Gough, K. (2007). Dense-core and diffuse Abeta plaques in TgCRND8 mice studied with synchrotron FTIR microspectroscopy. Biopolymers *87*, 207–217.

Reed-Geaghan, E.G., Savage, J.C., Hise, A.G., and Landreth, G.E. (2009). CD14 and toll-like receptors 2 and 4 are required for fibrillar Abeta-stimulated microglial activation. J. Neurosci. *29*, 11982–11992.

Ruiz, A., Dols-Icardo, O., Bullido, M.J., Pastor, P., Rodríguez-Rodríguez, E., López de Munain, A., de Pancorbo, M.M., Pérez-Tur, J., Alvarez, V., Antonell, A., et al.; dementia genetic Spanish consortium (DEGESCO) (2014). Assessing the role of the TREM2 p.R47H variant as a risk factor for Alzheimer's disease and frontotemporal dementia. Neurobiol. Aging *35*, 444.e1–444.e4.

Schmid, C.D., Sautkulis, L.N., Danielson, P.E., Cooper, J., Hasel, K.W., Hilbush, B.S., Sutcliffe, J.G., and Carson, M.J. (2002). Heterogeneous expression of the triggering receptor expressed on myeloid cells-2 on adult murine microglia. J. Neurochem. *83*, 1309–1320.

Song, M., Jin, J., Lim, J.-E., Kou, J., Pattanayak, A., Rehman, J.A., Kim, H.-D., Tahara, K., Lalonde, R., and Fukuchi, K. (2011). TLR4 mutation reduces microglial activation, increases Aβ deposits and exacerbates cognitive deficits in a mouse model of Alzheimer's disease. J. Neuroinflammation *8*, 92.

Stalder, M., Deller, T., Staufenbiel, M., and Jucker, M. (2001). 3D-Reconstruction of microglia and amyloid in APP23 transgenic mice: no evidence of intracellular amyloid. Neurobiol. Aging *22*, 427–434.

Stine, W.B., Jr., Snyder, S.W., Ladror, U.S., Wade, W.S., Miller, M.F., Perun, T.J., Holzman, T.F., and Krafft, G.A. (1996). The nanometer-scale structure of amyloid-beta visualized by atomic force microscopy. J. Protein Chem. *15*, 193–203.

Ulrich, J.D., Finn, M.B., Wang, Y., Shen, A., Mahan, T.E., Jiang, H., Stewart, F.R., Piccio, L., Colonna, M., and Holtzman, D.M. (2014). Altered microglial response to Aβ plaques in APPPS1-21 mice heterozygous for TREM2. Mol. Neurodegener. *9*, 20.

Wang, Y., Cella, M., Mallinson, K., Ulrich, J.D., Young, K.L., Robinette, M.L., Gilfillan, S., Krishnan, G.M., Sudhakar, S., Zinselmeyer, B.H., et al. (2015). TREM2 lipid sensing sustains the microglial response in an Alzheimer's disease model. Cell *160*, 1061–1071.

Yuan, P., and Grutzendler, J. (2016). Attenuation of β-Amyloid Deposition and Neurotoxicity by Chemogenetic Modulation of Neural Activity. J. Neurosci. *36*, 632–641.

Neuron, Volume *90*

Supplemental Information

TREM2 Haplodeficiency in Mice and Humans Impairs the Microglia Barrier Function Leading to Decreased Amyloid Compaction and Severe Axonal Dystrophy

Peng Yuan, Carlo Condello, C. Dirk Keene, Yaming Wang, Thomas D. Bird, Steven M. Paul, Wenjie Luo, Marco Colonna, David Baddeley, and Jaime Grutzendler

TREM2 haplodeficiency in mice and humans impairs the microglia barrier function leading to decreased amyloid compaction and severe axonal dystrophy

Supplemental Information

Peng Yuan[1,2*], Carlo Condello[1*#], C. Dirk Keene[3], Yaming Wang[4], Thomas D. Bird[5], Steven M. Paul[6], Wenjie Luo[6], Marco Colonna[4], David Baddeley[7,8], Jaime Grutzendler[1,2§]

1) Department of Neurology, Yale University, New Haven, CT 06510, USA
2) Department of Neuroscience, Yale University, New Haven, CT 06511, USA
3) Department of Pathology, University of Washington, Seattle, WA98195, USA
4) Department of Pathology and Immunology, Washington University School of Medicine, St. Louis, MO 63110, USA
5) Department of Neurology, University of Washington, Seattle, WA98195, USA
6) The Helen and Robert Appel Alzheimer's Disease Research Institute, Brain and Mind Research Institute, Weill Cornell Medical College, New York, NY10065, USA
7) Department of Cell Biology, Yale University, New Haven, CT 06511, USA
8) Nanobiology Institute, Yale University, West Haven, CT 06515, USA

*These authors contributed equally

#Present address: Department of Neurology, University of California San Francisco, 94158 USA

§Corresponding author: 300 George Street, 8300G, New Haven, CT 06511, jaime.grutzendler@yale.edu

Figure S1 (related to Figure 1)

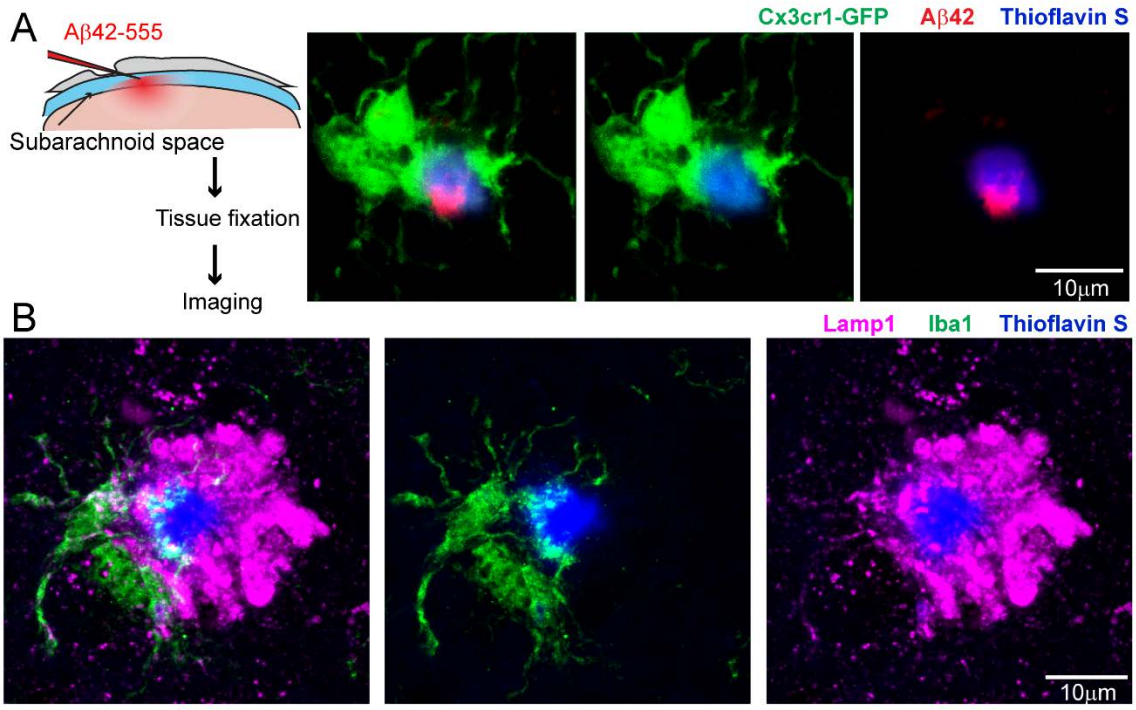

Microglia processes form a barrier that prevents toxic accumulation of Aβ42 hotspots leading to reduced neuritic dystrophy in microglia-covered areas.

(**A**) Soluble Aβ42 (red) preferentially incorporates into existing plaques (blue) at hotspot microregions lacking microglia barrier (green). Fluorescently labeled Aβ42 was infused into the subarachnoid space as described and tissue was fixed for imaging. Areas not covered by microglia have greater Aβ42 binding because the density of amyloid fibrils is lower (Condello et. al. 2015). The precise reason for the greater affinity to these uncovered areas is not clear. (**B**) Areas covered by microglia processes (green) are associated with less axonal dystrophy (labeled by a Lamp1 antibody; magenta) around plaques (blue). Neuronal processes near areas not covered by microglia processes are exposed to higher concentrations of toxic protofibrillar Aβ42 which leads to greater neuritic injury (Condello et. al. 2015).

Figure S2 (related to Figure 1)

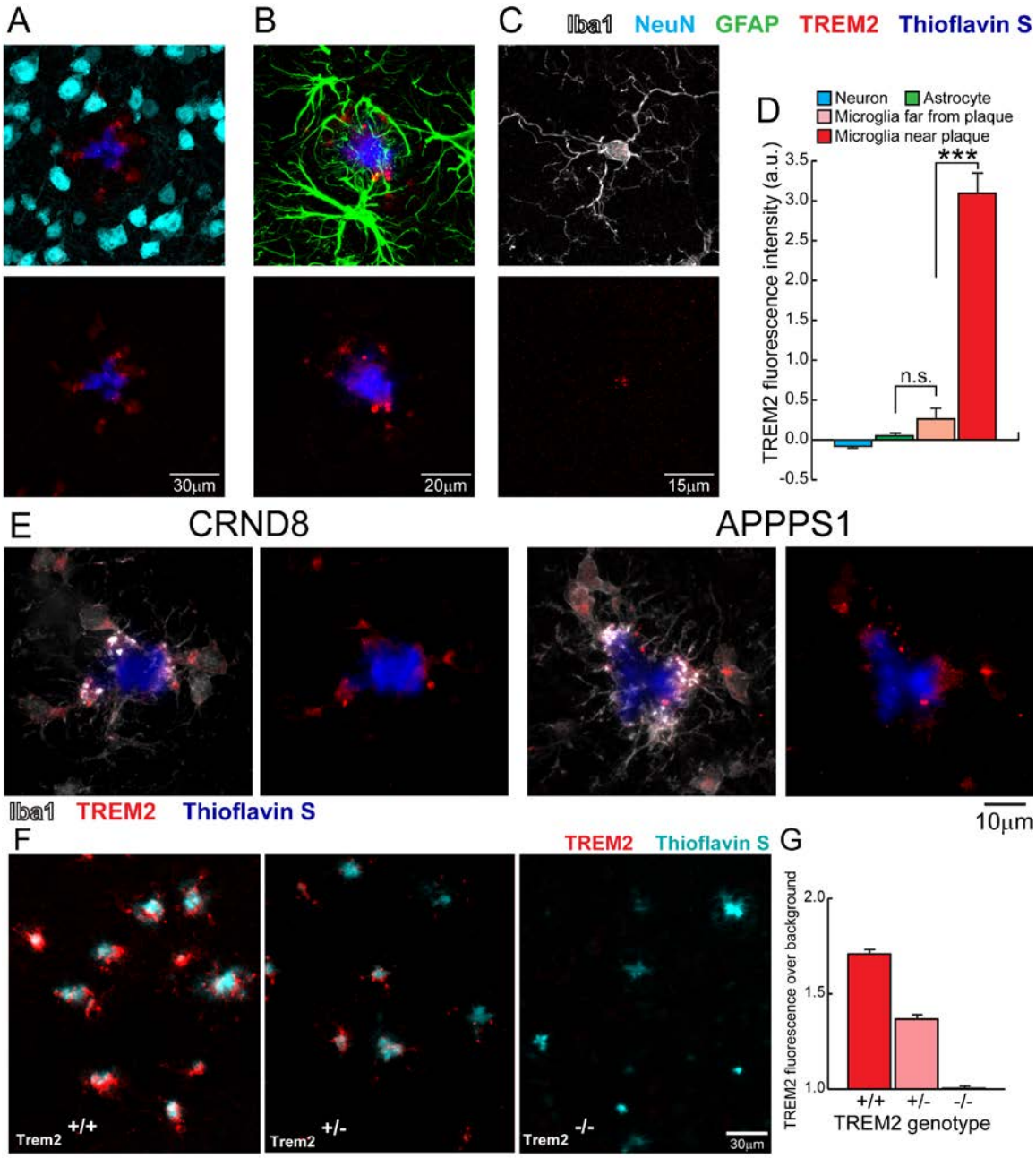

Trem2 is preferentially upregulated in plaque-associated microglia

Confocal images showing lack of Trem2 immunoreactivity within NeuN-labeled neurons (**A**) and GFAP-labeled astrocytes (**B**). Iba1-labeled microglia (white) far from plaques (**C**) have minimal Trem2 expression in the cell soma. (**D**) Quantification of fluorescence intensity of Trem2 in different cell types. N=3 animals, 150 neurons, 117 astrocytes and 150 microglia were analyzed. (**E**) Additional examples of Trem2 staining in CRND8 and APPPS1 transgenic AD mouse models. (**F**) Example images of Trem2 immunostaining in 5XFAD mice with Trem2 +/+, Trem2 +/- and Trem2 -/- genotype. (**G**) Quantification of Trem2 fluorescence intensity in brains of 5XFAD mice with different copy numbers of the Trem2 gene. N=3 mice

for each group. One-way ANOVA with post-hoc Tukey tests were used for statistical comparisons, ***: $p<0.001$, n.s.: $p>0.05$.

Figure S3 (related to Figure 2 and Figure 4)

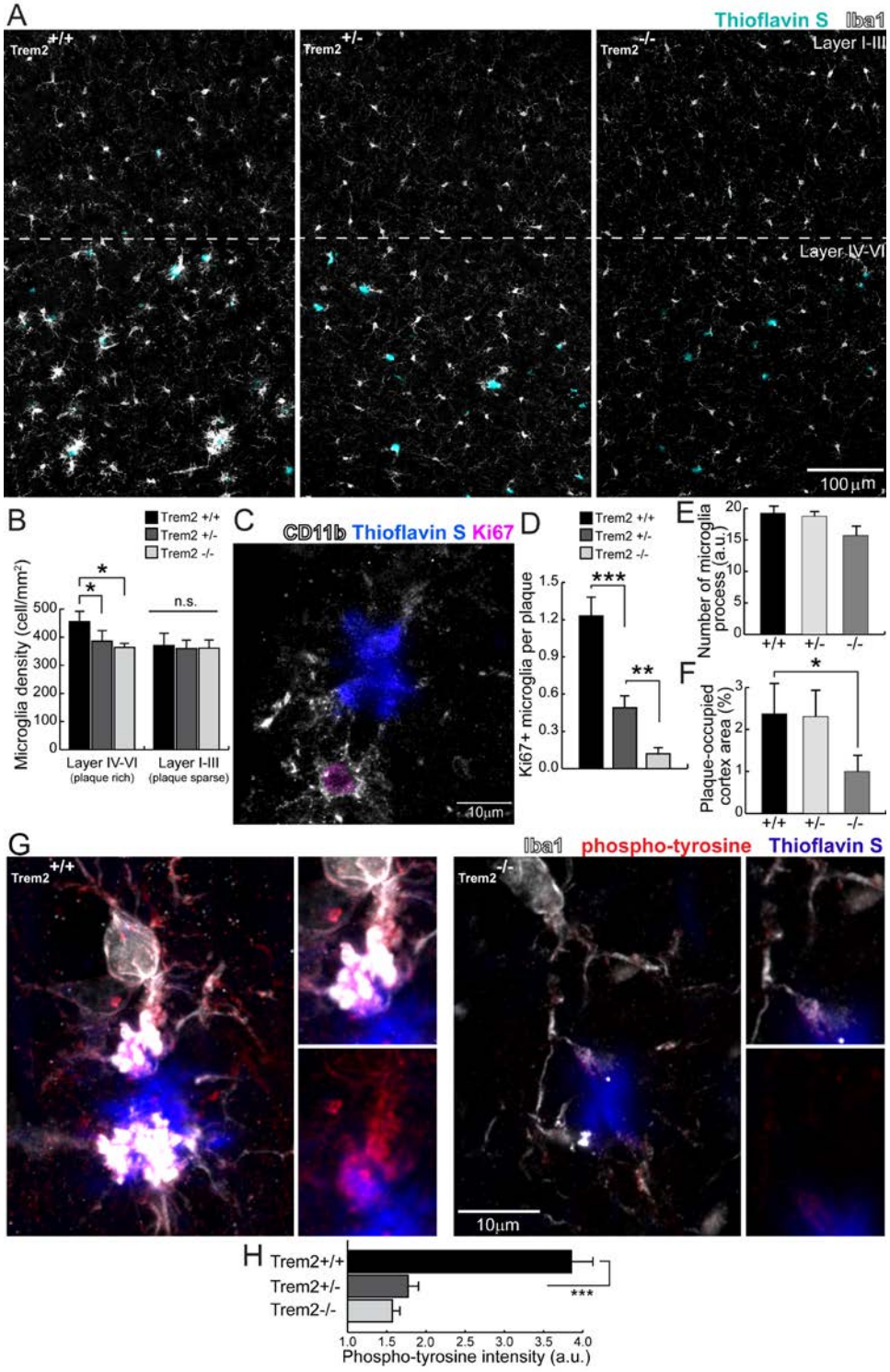

Trem2 deficiency diminishes the proliferative capacity of microglia in plaque-rich regions

(**A**) Confocal images of Iba1-immunolabeled microglia (white) thioflavin-positive amyloid plaques (cyan) in 5XFAD mice with different copy numbers of the Trem2 gene. (**B**) Cell number quantification of microglia in plaque-rich cortical layers IV-VI compared to plaque-free cortical layers I-III. N=3 mice for each group, total 1993 microglia analyzed. (**C**) Confocal images of proliferation marker Ki67-immunohistochemistry (magenta) within Iba1-immunopostive microglia (white) around thioflavin s-positive amyloid plaques (blue). (**D**) Quantification of Ki67-positive proliferating microglia per plaque in 5xFAD mice with different Trem2 genotypes. (**E**) Quantification of the amount of microglia processes around individual cell soma as measured by thresholded area of Iba1-immunolabeled processes. N=3 mice for each group, total 540 microglia were analyzed. See also **Figure 2**. (**F**) Quantification of total cortical area occupied by 4G8 positive amyloid plaques in 5XFAD mice with different copy numbers of Trem2 gene. Two brain slices were analyzed for each mouse and N=3 mice for each group. See also **Figure 4**. (**G**) Confocal images of phospho-tyrosine immunoreactivity (red) in plaque-associated Iba1-positive microglia (white) around thioflavin S-positive amyloid plaques (blue) microglia in Trem2 +/+ (left panels) and Trem2 -/- (right panels) 5xFAD brain slices. (**H**) Quantification of phospho-tyrosine levels in plaque-associated microglia in 5xFAD mice with different Trem2 genotypes. N=3 mice for each group, 450 cells were analyzed. One-way ANOVA with post-hoc Tukey tests were used for statistical comparisons in panels (**B**) and (**D**), and Student's t-tests were used in panels (**F**) and (**H**), *: $p<0.05$, ***: $p<0.001$; a.u.: arbitrary unit. All analyses were performed with neocortical plaques.

Figure S4 (related to Figure 2)

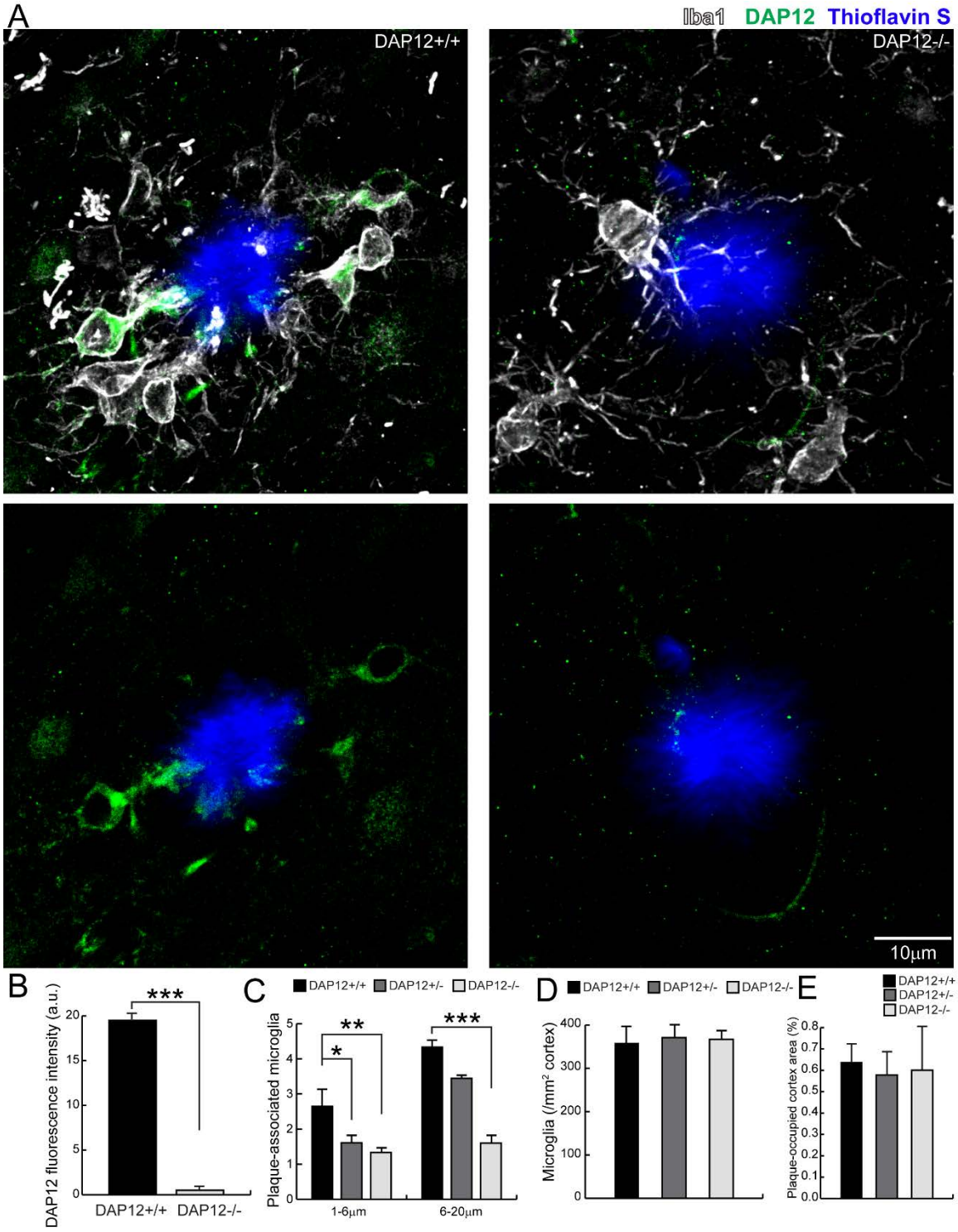

DAP12 deficiency abolishes microglia recruitment around amyloid plaques

(**A**) Confocal images of DAP12 staining within the Iba1-immunolabeled microglia (white) around thioflavin-positive amyloid plaques (blue) in APPPS1 mice with and without DAP12 gene. (**B**) Quantification of DAP12 fluorescence around amyloid plaques in DAP12 +/+ and -/- mice. 30 plaques were analyzed for each group. (**C-D**) Quantification of the number of microglia cells associated and far away from amyloid plaques. Total 163 plaques were analyzed. For all quantifications N=3 animals for each group. Student t-test was used for statistical comparison in panel (**B**), and One-way ANOVA with post-hoc Tukey tests were used separately for size groups in panel (**C**), *: $p<0.05$, **: $p<0.01$, ***: $p<0.001$; a.u.: arbitrary unit. All analyses were performed with neocortical plaques. (**E**) Quantification of the total percentage cortical area occupied by amyloid plaque in APPPS1 mice with and without DAP12 gene. Amyloid plaques were stained with 4G8 immunohistochemistry. Two brain slices were analyzed for each mouse and N=3 animals for each group.

Figure S5 (related to Figure 3)

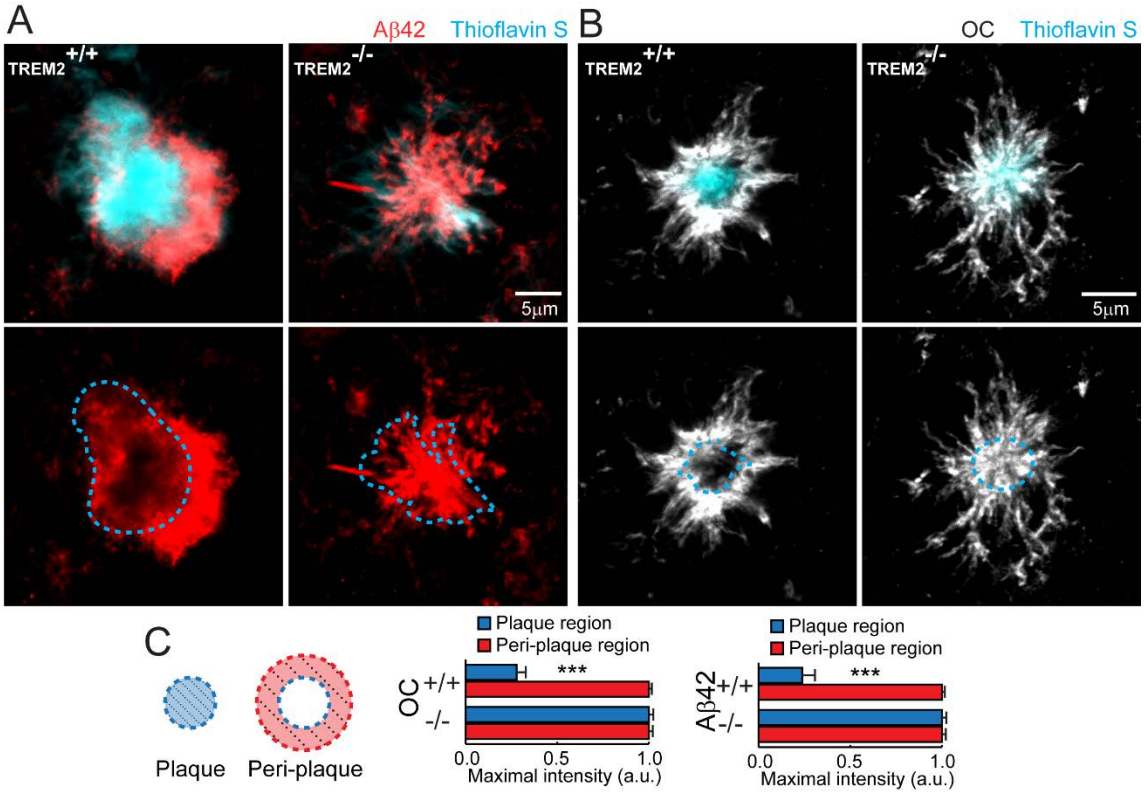

TREM2 deficiency reduces plaque compactness as revealed by increased penetration of Aβ antibodies to the plaque core

(**A** and **B**) Confocal images of anti-Aβ42 (red) and anti-oligomeric amyloid (OC; white) immunohistochemistry of thioflavin S positive plaques (cyan) in 5XFAD brain tissue with different Trem2 genotypes. Lower panels show fluorescence channel with antibody staining only. Cyan dashed lines indicate thresholded plaque perimeter (core). (**C**) Quantification of anti-Aβ42 and anti-OC antibody staining within plaque core and peri-plaque regions in Trem2+/+ and Trem2-/- mice. N=10 plaques in each group. One-way ANOVA with post-hoc Tukey tests were used for statistical comparison. ***: $p<0.001$; a.u.: arbitrary unit. All analyses were performed with neocortical plaques.

Figure S6 (related to Figure 6)

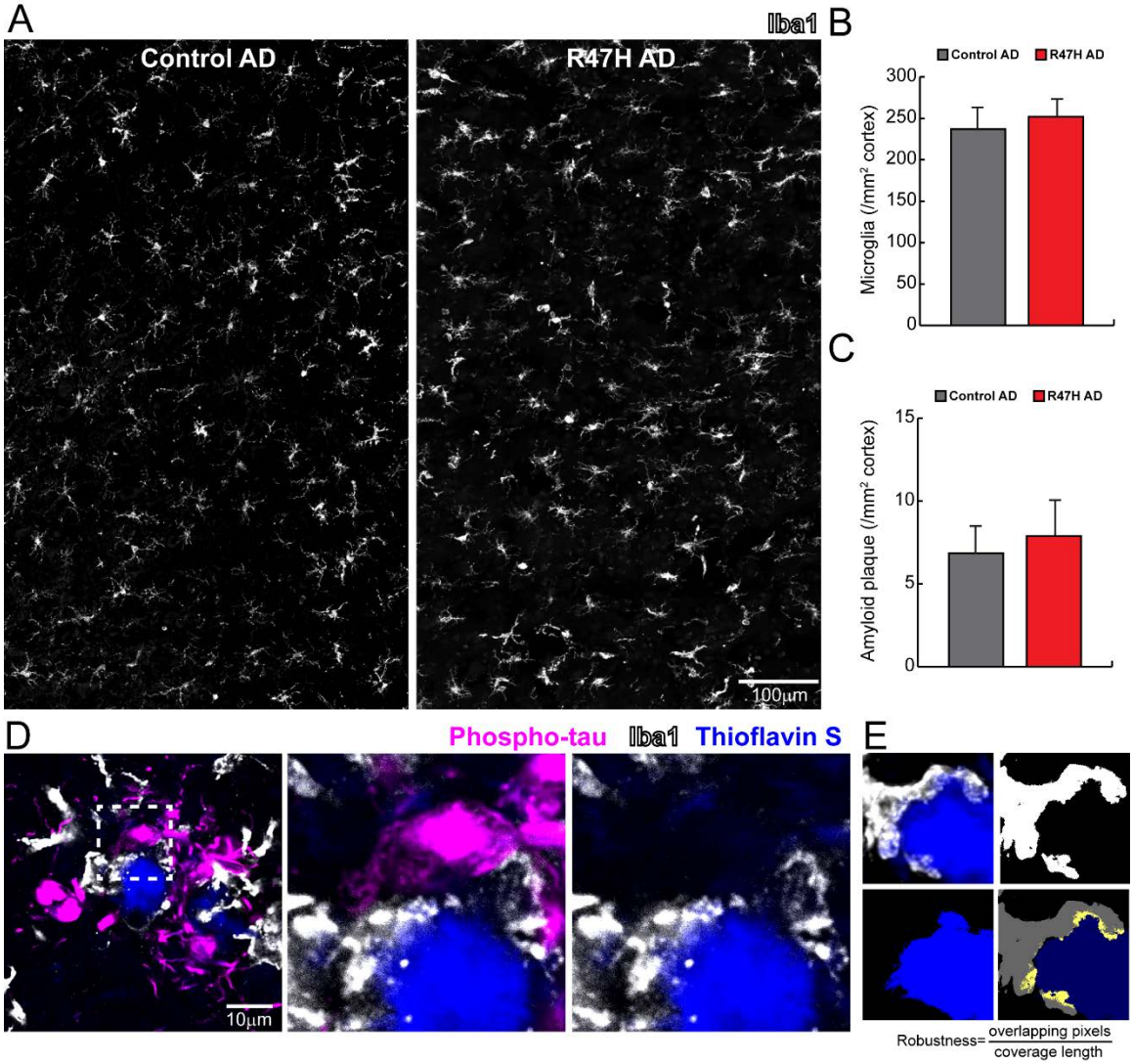

R47H TREM2 mutation disrupts microglia envelopment of amyloid plaques but has no effect on resting state microglia nor overall plaque burden

(**A**) Confocal images of microglia, labeled by anti-Iba1 immunostaining (white), in plaque-free cortical regions from postmortem human brains with and without R47H mutation. (**B**) Quantification of the number of microglia in cortical regions of human brains with and without R47H mutation. (**C**) Quantification of the number of plaques (all subtypes) in gray and white matter of human brains with and without R47H mutation. N=5 human subject for all quantifications. No statistical significance was detected using Student T-test. (**D**) Images of the stereotypical interaction between microglia and amyloid plaques. Microglia (anti-Iba1 labeling, white) spread their processes closely onto plaque (blue) surfaces, while they do not display any obvious interaction with adjacent dystrophic neurites (anti-phospho-tau labeling, magenta). Middle and right panels show zoomed split channel images from dashed box in the left panel. (**E**) Example of image processing to measure the "closeness" of the interaction between microglia processes and the amyloid plaque surface as "Barrier Robustness", see quantification in **Figure 6H**. Robustness was calculated as the number of overlapping pixels between microglia process and amyloid plaques (yellow pixels in the right bottom panel) normalized by the length of the plaque perimeter covered by the microglia process.

Figure S7 (related to Figure 6 and 7)

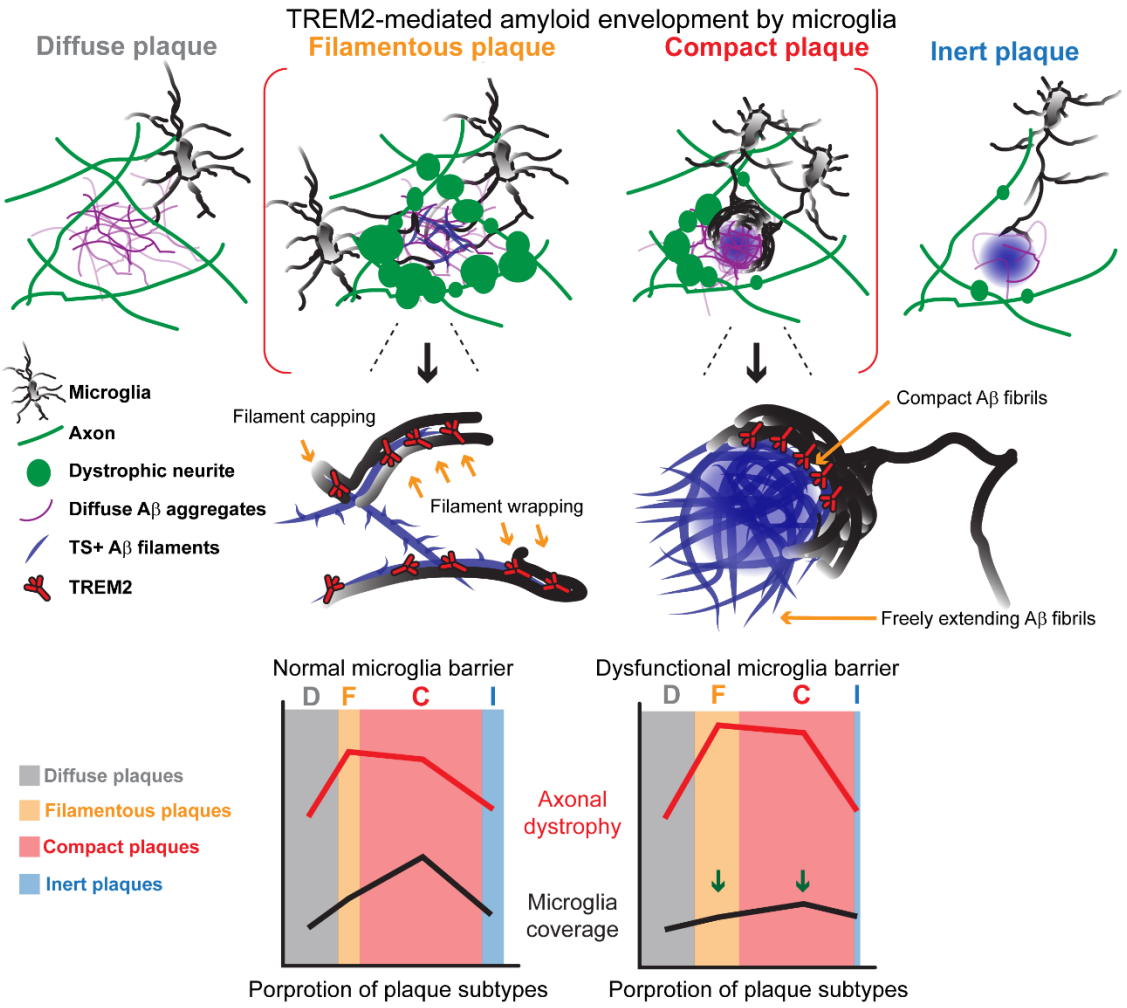

Summary diagram of microglia barrier function and molecular control by TREM2

1) Unlike diffuse amyloid plaques (thioflavin S negative), early filamentous amyloid deposits (thioflavin S positive) extensively attract polarized microglia processes that intermingle with it.

2) Diffuse plaques do not have dystrophic neurites around them while filamentous plaques have a surprisingly large degree of neuritc dystrophy suggesting that adoption of a beta-sheet rich conformation triggers axonal toxicity.

3) TREM2-rich microglia processes closely envelope individual thioflavin S positive amyloid filaments and small fibril clusters. Compact amyloid plaques are also robustly covered my microglia processes.

4) This interaction leads to thicker and shorter amyloid fibril bundles with reduced branching and to more compact amyloid deposits.

5) TREM2 haplodeficiency in humans and in mice causes a severe abnormality in the ability of microglia to polarize towards amyloid deposits. This leads to a more branched and less compact plaque phenotype with an overall increase in fibril surface area contacting adjacent neuronal processes. In both filamentous and compact plaques, the decreased compaction and increased fibril surface area caused by TREM2 haplodeficiency was associated with marked increases in the degree of axonal dystrophy and neuritic tau

hyper-phosphorylation. This strongly suggests that microglia envelopment of amyloid deposits plays a critical neuroprotective role by compacting toxic fibrils and insulating from the adjacent neuropil (Microglia “barrier function”).

6) In humans, we observed a subpopulation of plaques that had extremely high thioflavin S labeling and lacked enveloping microglia processes. Interestingly, these plaques demonstrated very little neuritic dystrophy. This suggests two possible explanations: one in which these are terminal plaques in which axonal dystrophy has peaked and subsequently disappeared due to degeneration. A second and more intriguing hypothesis is that these plaques were highly compacted at early stages such that very little dystrophy developed around them, and microglia no longer get attracted to them due to their exceptional degree of compaction.

7) Loss of the protective microglia barrier function in TREM2 deficiency does not change the total number of amyloid deposits, but instead leads to an increased proportion of filamentous plaques. Dysfunctional microglia barrier in TREM2 haplodeficiency and potentially due to microglia senescence in sporadic AD leads to more severe axonal dystrophy around amyloid deposits.

Table S1 (related to Figure 1)

	Vendor	Clone	Host	Species	Cat#	IHC result
Trem2	Santa Cruz	B-3	mouse	human	sc-373828	-
	Santa Cruz	G-16	goat	human	sc-22634	-
	R&D Systems		sheep	mouse	AF1729	+++
	Abcam		goat	human	ab85851	-
DAP12	Santa Cruz	A-20	goat	human; mouse	sc-7855	-
	Santa Cruz	C-20	goat	human; mouse	sc-7853	-
	Santa Cruz	FL-113	rabbit	human; mouse	sc-20783	-
	LS Bio		goat	human; mouse	B3718	-
	LS Bio		rabbit	mouse; human	B9453	++

Trem2 and DAP12 antibodies tested in this study

Heat-induced sodium citrate antigen retrieval was performed for all the antibodies tested with the following protocol: tissue was boiled in 50mM sodium citrate solution with 0.05% tween-20 at 95 degrees for 45 minutes and then washed with PBS 3 times before staining.

Table S2 (related to Figure 6 and 7)

Case ID	TREM2 R47H	Gender	Age	Braak Stage	Brain bank	Comorbid pathology
0013	Mutant	Male	87	V	BSHRI	Lewy body disease
0414	Mutant	Female	76	VI	UW-ADRC	
1462	Mutant	Female	89	V	UW-ADRC	Lewy body disease
5168	Mutant	Female	87	VI	UW-ADRC	Parkinson's disease; Meningitis
5219	Mutant	Male	86	VI	UW-ADRC	
0195	Control	Male	83	V	UW-ADRC	
0550	Control	Female	89	V	UW-ADRC	
1353	Control	Female	92	VI	BSHRI	Cerebral white matter rarefaction
1375	Control	Male	77	VI	BSHRI	Moderate Purkinje cell loss
1406	Control	Male	85	V	BSHRI	Microscopic infarct in left hippocampus
M6	Mutant	Female	87	V	MAYO	
M17	Mutant	Male	88	IV	MAYO	
M20	Mutant	Female	74	V	MAYO	
M21	Mutant	Male	76	VI	MAYO	
M22	Mutant	Female	77	VI	MAYO	Lewy body disease
M6c	Control	Female	84	IV	MAYO	
M20c	Control	Female	77	VI	MAYO	
M21c	Control	Male	74	V	MAYO	
M22c	Control	Female	83	V	MAYO	Lewy body disease

Donor information of the postmortem human AD brain tissues used in this study

All cases were confirmed with amyloid pathology in the brain tissue. All cases used in this study were Caucasians with the ApoE3/E4 genotype. Brain slices from the middle frontal gyrus (cortex) were used for all analyses in this study. BSHRI; Banner Sun Health Research Insitute (Sun City, AZ). UW-ADRC; University of Washington, Alzheimer's Disease Research Center (Seattle, WA). MAYO; Mayo Clinic (Jacksonville, FL).

Supplemental Experimental Procedures

Reagents

Anti-Iba1 polyclonal antibody (Wako, 019-19741, RRID:AB_839504), anti-Coronin1a (Santa Cruz, clone 14.1, sc-100925, RRID:AB_2291951) and anti-CD11b (AbD Serotec, clone 5C6, MCA711G, RRID:AB_323167) were used to label microglia. Anti-mouse TREM2 antibody (R&D systems, AF1729, RRID:AB_354956) was used to detect TREM2 protein. Anti-DAP12 antibody (LifeSpan Biosciences, LS-B9453, originally RRID:AB_10828136) was used for staining DAP12. Anti-Ki67 antibody (Abcam, ab16667, RRID:AB_302459) was used to label dividing cells. Anti-GFAP antibody (DAKO, Z0334, RRID:AB_10013382) was used to label astrocyte. Anti-NeuN antibody (EMD Millipore, ABN78, RRID:AB_11211087) was used to label neuronal nucleus. Anti-phospho-tyrosine antibody (EMD Millipore, clone 4G10, 05-321, RRID:AB_309678) was used to detect phosphorylated tyrosine. Anti-Lamp1 antibody (DSHB, 1D4B, RRID:AB_2134500) was used to label neuritic dystrophy in mice and anti-APP antibody (ThermoFisher Scientific, LN27 13-0200, RRID:AB_86542) and anti-Phospho-PHF-tau pSer202+Thr205 (ThermoFisher Scientific, AT8 MN1020, RRID:AB_223647) were used for human. Anti-Aβ 17-24, 4G8 antibody (BioLegend, 800701, RRID:AB_2564633) was used to label amyloid plaques. Anti-CD68 antibody (AbD serotec, MCA1957, RRID:AB_322219) was used to label microglial phagosomes. Alexa dye conjugated secondary antibodies were used (ThermoFisher Scientific). For STORM microscopy (see below), anti-Aβ antibody (Cell Signaling Technology, #2454, RRID:AB_2056585) and goat anti-rabbit-Alexa 647 secondary antibody (ThermoFisher Scientific, A-20991, RRID:AB_2535705) were used to label amyloid fibrils. Thioflavin S (Sigma-Aldrich, T1892, 2% w/v stock solution, 1:10k staining) was used for labeling amyloid deposits in fixed slices. DAPI (Sigma-Aldrich, D9542) was used for labeling cell nuclei.

Confocal analyses

Measurements of plaque sizes were collected using z-axis projections of 5 optical slices aligned along the center of the plaques. Plaque regions were distinguished using a threshold fluorescence intensity that was two standard deviations above the average fluorescence intensity of the image as previously reported. Classification of thioflavin S positive or negative plaques were done by scrolling through the z-stack and

judging manually. Only plaques that were completely within the whole depth of the z-stack were counted in this analysis.

Microglia barrier around filamentous plaques was defined as 1) processes closely tracking along and wrapping around individual amyloid fibril and 2) processes forming cap-like structures at the end of amyloid filament. These events were manually quantified from the whole z-stack of individual plaque. Microglia barrier around compact plaques was defined as activated microglia processes tightly wrapping around amyloid plaques, with Iba1 expression higher than the baseline microglial processes. In order to measure the compact plaque coverage by microglia barrier, a 3-slice z-projection at the center of the segmented plaque was made. The Iba1 channel was then thresholded using the Iba1 fluorescence intensity in the cell body as the cutoff value. The contact points of plaque perimeters with microglia processes was then determined manually. And the proportion of the plaque perimeter covered by microglia barrier was determined by measuring the distances between contact points along plaque perimeter. For measuring barrier robustness, theresholded images were generated for both the Iba1 and thioflavinS channel. The number of pixels overlapping between the two channels were counted and then divided by the plaque perimeter covered by microglia barrier.

For measuring dystrophic neurites, a 3-slice z-projection through the center of the plaque core was made for each segmented plaque. The dystrophy area was determined by threshold the image with 150% fluorescent intensity of a background region in the same channel. To estimate the volume of dystrophy, the measured area was converted to volume assuming a spherical geometry. Plaque volume was subtracted from the dystrophy volume.

For measuring the degree of dystrophic neurites corresponding to microglia covered and not covered plaque microregions, the total area of dystrophic neurites was radially divided into pie-shaped regions based on microglia coverage. A pie-shaped selection was made by connecting the center of the plaque and the points used for measuring microglia barrier, and extending outward until crossing the dystrophic neurites border. Subsequently, the area of dystrophic neurites was measured within each pie-shaped selection and assigned to microglia covered and not covered regions. The assigned area of dystrophic neurites was further normalized by the degree of microglia coverage:

$$Dystrophic\ neurite\ (covered/\ not\ covered) = \frac{\frac{Dystrophy\ area\ in\ covered\ regions}{Microglia\ coverage}}{\frac{Dystrophy\ area\ in\ not\ covered\ regions}{(360 - Microglia\ coverage)}}$$

If the above ratio is less than 1, it indicates the microglia coverage is relatively protective in preventing dystrophic neurites around plaques. Geometric mean of all the plaques measured in each subject was used as the average measurement for each person.

For measuring Trem2 immunostaining, fluorescence intensities were measured from a 5μm z-projection through the center of desired structure. The region of interest was determined by manual tracing. To measure phosphor-tyrosine fluorescence intensities, a selection of 4μm width was created along the perimeter of the plaque, using the "XOR" function between "Enlarge" +2 and -2 regions.

For measuring thioflavin S fluorescent intensity and circularity, a z-projection of maximal fluorescence intensities across 5 optical slices through the center of the plaque core was made. The plaque area was selected by "isodata" threshold and thioflavin S fluorescent intensity was measured from the selection. The selection was also used to calculate circularity by the following equation: circularity = 4π x area / $(\text{perimeter})^2$.

For measuring microglia polarization, microglia cells were segmented from the tiled images described above. A z-projection at the center of the cell body was made across 5 optical sections. The somata of microglia was traced manually and the cell's territory was selected using "Enlarge" function in FIJI at 20μm. The donut shape selection was divided radially into 8 pies, each representing roughly 45 degree space surrounding the cell. Fluorescence intensity of Iba1 staining was measured in each of the 8 pie areas and polarization index was calculated as the coefficient of variation for the 8 regions (ratio of the standard deviation to the mean). In addition to fluorescence intensity, thresholded area of the Iba1 staining was also analyzed in the same method and the results were consistent with using fluorescence intensity (not shown).

For measuring Aβ phagocytosis by microglia, a z-projection was made for each microglia to cover the total volume of the somata. The CD68 fluorescent channel was thresholded using "IsoData" preset in FIJI and total area was measured using "Analyze Particle" function. The 4G8 fluorescent channel was also

thresholded using “IsoData” and the intra-microglia amyloid was measured by multiplying the 4G8 puncta area and the fluorescence intensity.

STORM analyses

Reconstructed images were imported into FIJI via “BioFormat” plugin for analyses. Images were converted to 16-bit before measurements. To measure different fibril organization areas in each plaque, the image was first thresholded with “isodata” to measure the total area of the plaque. Subsequently, the compact core areas were manually traced based on the marked differences in fluorescence intensity. Next, the mesh-like structures were traced based on the definition where fibril directions cannot be determined confidently. Diffuse fibril areas were then calculated by subtracting these two compact areas from the total area of the plaque.

To measure the width of individual Aβ fibril, a 10-pixel wide line selection was made horizontally from the fibril. Fluorescence intensity profiles from the line was recorded and plotted against distance. The plotted line was then fitted with a Gaussian curve and width was determined by 2.35 times of the standard deviation of the fitted curve.

To measure the frequency of the branched structures, single segments of fibrils without intersecting with other fibrils were chosen. Branched structure was defined as fibrils orthogonally extending from the main Aβ fibril stem. The tip of the branches needs to exceed 8 pixels (~40nm) away from the main fibril in order for this structure to be counted.

Estimation of plaque surface area change in Trem2 deficient mice

The following equations are used to estimate the surface area:

Surface area = Surface area of individual fibril * Number of diffuse fibrils.

Surface area of individual fibril = (π * (fibril diameter) * (fibril length)) + surface area of individual branched structure * Densities of branched structures * fibril length

From our STORM imaging results, average fibril diameter in Trem2 +/+ is 67nm, Trem2 +/- is 56nm and Trem2 -/- is 46nm, length +/+ 231nm, +/- 396nm, -/- 442nm.

Next in order to estimate the area of individual branched structures, we assume the average dimensions of these structures are 20nm in diameter and 80nm in length. Therefore surface area of individual branch structure = $\pi * 20 * 80$ $(nm)^2$. The densities of branched structures in Trem2 +/+ is 0.5, Trem2 +/- is 2.1 and Trem2 -/- is 3.2, per 500nm length of fibril.

Therefore the surface area of individual fibrils can be calculated:

Trem2 +/+: $(\pi * 67 * 231) + (\pi * 20 * 80 * 0.5 / 500 * 231) = 49{,}756$ $(nm)^2$

Trem2 +/-: $(\pi * 56 * 396) + (\pi * 20 * 80 * 2.1 / 500 * 391) = 77{,}988$ $(nm)^2$

Trem2 -/-: $(\pi * 46 * 442) + (\pi * 20 * 80 * 3.2 / 500 * 442) = 78{,}054$ $(nm)^2$

This can be normalized to Trem2 +/+ 100%, Trem2 +/- 157% and Trem2 -/- 157%.

Next, Number of diffuse fibrils is estimated assuming equal amount of amyloid material for each plaque. Our results indicate that 30% of the total material in Trem2 +/+ are diffuse fibrils, 60% in Trem2 +/- and 85% in Trem2 -/-. This translates to 2 times in the number of fibrils in Trem2 +/- and 2.83 times in Trem2 -/- compared to Trem2 +/+.

Taken together, we estimate Trem2 +/- increased surface area of individual plaque to 157% * 2 = 314% and Trem2 -/- to 157% * 2.83 = 444% compared to Trem2 +/+.